A comparison of WRF simulated composite reflectivity and precipitation to observations in the Central US

A Thesis Submitted to the College of Graduate and Postdoctoral Research in partial fulfillment of the requirements for the Degree of Master of Environment and Sustainability in the School of Environment and Sustainability University of Saskatchewan Saskatoon

By
Jason Flemke

University of Saskatchewan Permission to Use

In presenting this thesis in partial fulfillment of the requirements for a graduate degree from the University of Saskatchewan, I agree that the libraries of this university may make it freely available for inspection. I further agree that permission for copying this thesis in any manner, in whole or in part, for scholarly purposes may be granted by the professor who supervised my thesis work, or in their absence, by the head of the department or the dean of the college in which my thesis work was done. It is understood that any copying or publication or use of this thesis or parts thereof for financial gain shall not be allowed without my written permission. It is also understood that due recognition shall be given to me and to the University of Saskatchewan in any scholarly use which may be made of any mater al in my thesis. Request for permission to copy or to make other use of the material in this thesis in whole or in part should be addressed to:

Executive Director
School of Environment and Sustainability
University of Saskatchewan
Room 329, Kirk Hall
117 Science Place
Saskatoon, Saskatchewan S7N 5C8
Canada

OR

Dean
College of Graduate and Postdoctoral Studies
University of Saskatchewan
116 Thorvaldson Building, 110 Science Place
Saskatoon, Saskatchewan S7N 5C9
Canada

Abstract

Precipitation from Mesoscale Convective Systems (MCSs) in the central US are not only a large contributor to water resources, but a hazard to society due to hail, wind gusts, tornadoes, lightning, and flash floods. These severe storms can cause damage to houses, vehicles, and trees. Due to this significance, there is a large interest in using Numerical Weather Prediction (NWP) to predict extreme weather and climate. Also, with a changing climate, it is important to understand how weather system characteristics will change in the future.

Convection-permitting NWP models simulate convective processes more realistically than coarser grid models due to errors in local-scale processes and convective parameterization not accurately producing convection. The National Center for Atmospheric Research (NCAR) conducted a continental-scale convection-allowing simulation using the regional Advanced Research Weather Research and Forecasting (WRF-ARW) model. The model simulations are made up of two parts: (1) A 13-year (2000–2013) simulation of historical weather and climate patterns, and (2) A pseudo global warming (PGW) simulation to project the weather and climate patterns at the end of the 21st century. This model was designed to have 4-km grid spacing covering the entire continental US and the southern portion of Canada (up to 56 ºN) and downscaled the ERA-Interim reanalysis for the period from October 2000 to September 2013. Downscaling to a higher resolution permits the model to simulate deep convection without parameterization, proving to be more realistic.

The primary objective of this study is to evaluate the historical portion of the WRF model's capabilities in producing the characteristics of observed warm-season convection in the central United States, with an emphasis on radar reflectivity distribution, the diurnal cycle of precipitation and storm propagation. The secondary objective is to evaluate the PGW projection to understand how a future climate will impact radar reflectivity distribution, the diurnal cycle of precipitation, and storm propagation. The first objective is achieved by comparing the simulated composite (column maximum) radar by comparing the Weather Surveillance Radar-1988 Dopplers (WSR-88Ds) national mosaic is an objective of this research. Along with radar, the accumulated modeled precipitation is validated against the Stage IV multisensory gridded observed precipitation product. The comparison focuses on the central plains of the US for March through August. Specifically, the area of interest for this research is between 30 ºN and 45 ºN, and 90 ºW and 105 ºW.

Results comparing the historical simulation to observations show that the simulation can produce a similar distribution of heavy extreme reflectivity values, yet is shown to underestimate light and moderate reflectivity and precipitation frequencies. This study also determined that the model can capture the timing of the precipitation diurnal cycle, including the general propagation of thunderstorms across the domain. However, there is a significant underestimation of nocturnal convection in the central US east of the high plains. These model deficiencies are partly due to small (> 4km) scale forcing mechanisms (i.e., cold pool propagation and undular bores) that play a role in nocturnal initiation of convection and the warm/dry bias present in the simulation during JJA.

The research presented in this thesis illustrates that this convective permitting high-resolution WRF simulation is beneficial in understanding the precipitation patterns in the central US and possible effects of climate change on precipitation. However, the warm and dry bias present in the central US, lack of simulated small scale forcing mechanisms, and the PGW simulation not including the change in climate storm track dynamics should be considered as model weaknesses. This study concludes that this simulation can be more useful by improving the land surface and radiation schemes, improve the parameterization of small scale mechanisms and use a smaller horizontal grid spacing to simulate shallow convection better. This research should contribute to the climate modeling community since this is a high-resolution climate simulation that has shown to be a large improvement from coarse resolution climate models.

Keywords: Climate change, Convection-Permitting Model, Pseudo Global Warming, Radar, Precipitation Diurnal Cycle, Weather Research and Forecasting

Acknowledgments

I would like to firstly express my gratefulness and appreciation to my research supervisor, Professor Yanping Li for the valuable guidance, advice, and encouragement throughout the progress of this research work. I also express sincere thanks to the Advisory Committee members, Professors Andrew Ireson, and Huiqing Guo for their valuable comments and suggestion in the preparation of this thesis.

This research was made possible by the use of the computational resources (DOI:10.5065/D6RX99HX) at the NCAR-Wyoming Supercomputing Center provided by the National Science Foundation, the State of Wyoming, and supported by NCAR's Computational and Information Systems Laboratory. I also gratefully acknowledge the Global Water Futures (GWF) project and the Global Institute for Water Security (GIWS) at the University of Saskatchewan for the funding throughout this research project.

I would also like to acknowledge the support from the NCAR Research Applications Laboratory (RAL), specifically Kyoko Ikeda, Changhai Liu, Andreas Prein, and Roy Rasmussen. Many thanks also for the valuable support during this study from Lintao Li, Zhenhua Li, Lucia Scaff, Sopan Kurkute, Yunsung Hwang, and Zhe Zhang. I would also like to thank my friends and family for support and encouragement throughout my graduate studies.

Contents

List of Tables

List of Figures

List of Abbreviations

AOGCM	Atmosphere Ocean General Circulation Model
BET	Background Exceedance Test
CC	Correlation Coefficient
CMIP5	Coupled Model Intercomparison Project 5
CONUS	Contiguous United States
CPCM	Convective Permitting Climate Model
CTRL WRF	Control Run – Historical Climate
dBZ	Decibels of the radar reflectivity factor Z
ECMWF	European Centre for Medium range Weather Forecasts
ERA ECMWF	Re-Analysis
GCM	Global Climate Model
GHG	Greenhouse gases
HRAP	Hydrologic Rainfall Analysis Projection
IPCC	International Panel on Climate Change
JJA	June July August
LLJ	Low Level Jet
LST	Local Solar Time
MAM	March April May
MCS	Mesoscale Convective System
MP	MicroPhysics
NCAR	National Center for Atmospheric Research
NCEP	National Centers for Environmental Prediction
NEXRAD	Next-Generation Radar
NSSL	National Severe Storms Laboratory
NWP	Numerical Weather Prediction
RCM	Regional Climate Model
RCP	Representative Concentration Pathway
RRTMG	Rapid Radiative Transfer Model for GCMs
OBS	Observations

PECAN	Plains Elevated Convection At Night
PGW	Pseudo Global Warming
SRES	Special Report on Emissions Scenarios
STIV	Stage IV precipitation data
USGP	United States Great Plains
UTC	Coordinated Universal Time
WRF-ARW	Advanced Research Weather Research and Forecasting
WSR-88D	Weather Surveillance Radar 1988 Doppler
YSU	Yonsei University
ZR	Reflectivity to Rainfall Rate relationship

Chapter 1. Introduction

1.1 Background

The United States Great Plains (USGP) is one of four global future vulnerability hotspots for water availability from the 2030s and later (Liu et al. 2013). In the USGP, water withdrawals from increased irrigation would exceed 40% of freshwater resources (Liu et al. 2013). Convective thunderstorms contribute to approximately half of the warm season (March-August) precipitation that falls over the United States (Fritsch et al. 1986). Mesoscale Convective Systems (MCS's), which account for 30–70% of the total warm-season precipitation in the central U.S. (Feng 2016), are an abundant type of convection in this area. Since convective precipitation (>10 mm hr^{-1}) provides a majority of the water supply in the central U.S., about 70% of precipitation during approximately 25% of all rainy days (Groisman 2012), it is crucial to understand how this water source may change in the future.

As anthropogenic greenhouse gas concentrations increase in our atmosphere, the effects of climate change are becoming more prevalent. The Intergovernmental Panel on Climate Change (IPCC) 5^{th} Assessment Report (AR5) states that the increase of greenhouse gases is exceptionally likely to have been the leading cause of the observed warming since the mid-20th century (IPCC AR5 2014). The IPCC report also predicts that extreme precipitation events may become more intense and frequent in the central U.S. (Prein et al. 2016). The possible change in frequency and severity of thunderstorms will threat agricultural activities and increases the risk of economic loss. It is essential to understand how a warmer future climate will impact thunderstorms and how these storms will impact the Central United States society and their economic activities.

1.2 Research Gap

For decades, there has been ongoing research in the field of mesoscale meteorology and convective storms in the central U.S. There have been several studies investigating severe storms, the diurnal cycle of precipitation and modeling convection all with the goal to understand processes that produce mesoscale weather phenomena, and a principal objective to improve forecast and model accuracy. However, there is a need to properly investigate simulated radar reflectivity and

precipitation from regional climate models compared with observational datasets.

Many studies have been performed on MCS formation and its eastward propagation in the central U.S. (Augustine and Caracena 1994, Corfidi 2003, Moore et al. 2003). WRF models are mainly used in this topic of research to learn more about these processes that occur in the atmosphere. These models have been used to find the best model set up and parameterizations to more accurately simulate the initiation and propagation of convection in this area. However, the parameterization of convection leads to model biases of temperature and precipitation. Convective permitting models, such as the model used in this study, have been shown to substantially improve the representation of convection (Prein et al. 2015). This research will benefit the climate modeling field in learning more about and to improve modeling the central U.S. precipitation diurnal cycle and nocturnal convection.

The initial results of the WRF simulation used in this research were presented by Liu et al. (2016). The authors show that the WRF model successfully simulates the spatial and temporal precipitation and temperature patterns over most of the United States, but also under-predicts summertime precipitation greater than 10 mm hr^{-1} in the central U.S. With 4-kilometer horizontal grid spacing, the accuracy of simulating convection should improve, but some parts of the domain may still show biases. This research project plans to add to this analysis of convection in the central U.S. and will also confirm the model's capabilities in producing characteristics of observed warm-season convection to understand better how and why this bias occurs.

This research hopes to improve the understanding of this simulation deficiencies by comparing it to the historical climate. Modeling nocturnal propagating convection in the central U.S. has been a longstanding difficulty in the model research community. Ever since research found this statistical maximum in nocturnal precipitation leeward of the Rocky Mountains and windward of the Appalachian Mountains, modelers have attempted to simulate this in order to learn more about the mechanisms that produce storms in this area at night due to the considerable agriculture/economic impact precipitation has. The research gap here is in understanding why models have trouble with simulating nocturnal convection. Most climate models use convective parameterization, so a model with domain this size at 4-km horizontal resolution at climate scale has not had much research done. This study will benefit the regional climate model research field through increasing knowledge of explicitly simulating convection on a climate time scale and how to improve model deficiencies that occur.

Also, with the threat of climate change impacting this area of the U.S., a change in storm characteristics must be reviewed to understand how a shift in climate may affect the region. This

research hopes to learn from the simulation about how the future climate will behave with more greenhouse gases in the atmosphere. Many studies have used RCMs to project possible climate scenarios, but few have used models with high enough resolution to allow for the convective parameterization to be turned off. This 13-year regional climate model used in this study allows for convection to be resolved explicitly in the simulation. This study will also contribute to the sustainability field to gain an understanding of how a change in the central U.S. climate will impact precipitation, water resources, and the agriculture of this area.

The use of the PGW model approach has been successful in simulating a future climate (Schär et al. 1996, Kawase et al. 2009, Rassmussen et al. 2011), with the model in this study using similar model procedures. Central U.S. radar and precipitation research regarding the future projection of convective storms is an understudied topic. Utilizing this regional climate model will be a considerable step forward in understanding the impact an increase in greenhouse gases will have on the central U.S. climate. This research will contribute to the understanding of the potential impacts that will occur from severe weather and climate change in the future on the current 'business as usual' GHG emissions path.

1.3 Research Objectives

This research aims to evaluate the WRF model's capabilities in producing similar characteristics of observed warm-season convection in the central United States, with the emphasis on reflectivity distribution, the diurnal cycle of precipitation, and storm propagation. The primary objective is to analyze the simulated radar and precipitation in the WRF historical model and compare to the observed radar and precipitation data. We attempt to learn if the WRF model significantly differs from the observations and why. The secondary objective is to investigate the differences in the simulated radar and precipitation between the WRF PGW model and the historical WRF run (CTRL). We investigate how the historical simulated radar reflectivity and precipitation significantly differs from the WRF PGW simulated reflectivity and precipitation, as well as how precipitation from convection may become more frequent and more severe in a PGW climate projection.

1.4 Thesis Outline

The content of this thesis spans six chapters. Chapter two is a literature review of related

background and studies of weather, climate patterns, and climate modeling contributions and challenges. Chapter three describes the observation data and WRF simulation set up used for this research. The key findings of this study are presented in chapter four. Chapter five discusses the overall results including a climate change assessment discussion based on the secondary objective. Finally, chapter six presents an overall summary and concluding remarks. This thesis presents the details of the background of the study, the data utilized, and the methods that will be taken to study this regional climate model for the central United States.

Chapter 2. Literature Review

Due to the impact of severe thunderstorms and the importance of deep convection in the central US hydrologic cycle, considerable research has been done in the past to learn more about mechanisms that cause severe weather and simulations performed to improve the predictability of these storms. Convective permitting simulations have largely improved the accuracy of NWP models, but a common model deficiency still exists in simulating nocturnal convection. A large portion of research is also dedicated to studying future climate, especially with the impact of climate change due to the threat of rising greenhouse gases. This chapter presents the literature survey to review central US severe weather research and climate change projection studies that are related to this research study.

2.1 Mesoscale convection in the Central U.S.

As the Earth undergoes unequal heating from the Sun, convective thunderstorms develop to balance this difference in heating (Ahrens 2011). Convection in the atmosphere occurs when a parcel of air is convectively unstable, i.e., the air parcel is at a warmer temperature compared to the environment around it. As winter ends, the Earth begins to tilt toward the sun, causing more direct sunlight reaches the Earth. Hence, precipitation from convection most often takes place in the spring and summer months (March–August in the Northern hemisphere) (Ahrens 2011).

Different types of convective storms are classified based on their duration, size, and intensity (Ahrens 2011). The most common type is the single-cell thunderstorm, lasting just 30 minutes on average. When multiple storms are organizing together, it becomes a multi-cell thunderstorm. Depending on the atmospheric conditions, these storms may propagate together, persist for long periods, and may even develop severe characteristics. The supercell thunderstorm is another type of severe convection. Deep convection in a supercell can produce in high-speed winds, large hail, and tornado formation, resulting in damages to infrastructure and agriculture that cost billions of dollars (Lott and Ross 2006).

Since convection in the central U.S. is a crucial source of annual precipitation, a significant part of the research is done to improve the forecasting of severe storms for both short-term (weather forecasts) and long-term (climate projections). In most of the southern USGP, the annual peak

precipitation occurs in May (Bukovski et al. 2017), driven by the springtime instability from surface heating combined with moisture transported from the Gulf of Mexico and numerous disturbances forcing ascent to initiate convection. One example is how the cold, dry air from the Rocky Mountains meets warm moist air from the Gulf of Mexico, which are the two ingredients to create destructive severe thunderstorms. These conditions can frequently occur in spring and summer in the central United States, where 'Tornado Alley' is located (Bluestein 2006).

2.2 Mesoscale Convective Systems

A Mesoscale Convective System (MCS) is a large group (on the scale of a 100 km) of organized thunderstorms that persist for at least several hours. In the central U.S., MCSs contribute 30–70% of the average warm-season precipitation (Fritsch et al. 1986). Types of MCSs include squall lines, bow echoes, and tropical cyclones in their early formation. A common type of MCS that make up many of these storms is the Mesoscale Convective Complex (MCC), shown in Figure 2.1.

MCCs often traverse the central U.S. overnight originating from the leeward of the Rocky Mountains in the afternoon. This nocturnal convection is often studied and modeled to improve forecasting (Geerts et al. 2017, Reif and Bluestein 2017, Stelten and Gallus 2017). If the appropriate atmospheric conditions are present, an MCC will form, and after evening, the MCC will continue to propagate eastward overnight, which gives the MCCs the characteristics of the diurnal cycle. The majority of MCCs exhibit a nocturnal life cycle that begins in the mid-to-late afternoon, peaks after midnight, and ends shortly after daybreak (Laing and Fritsch 1996).

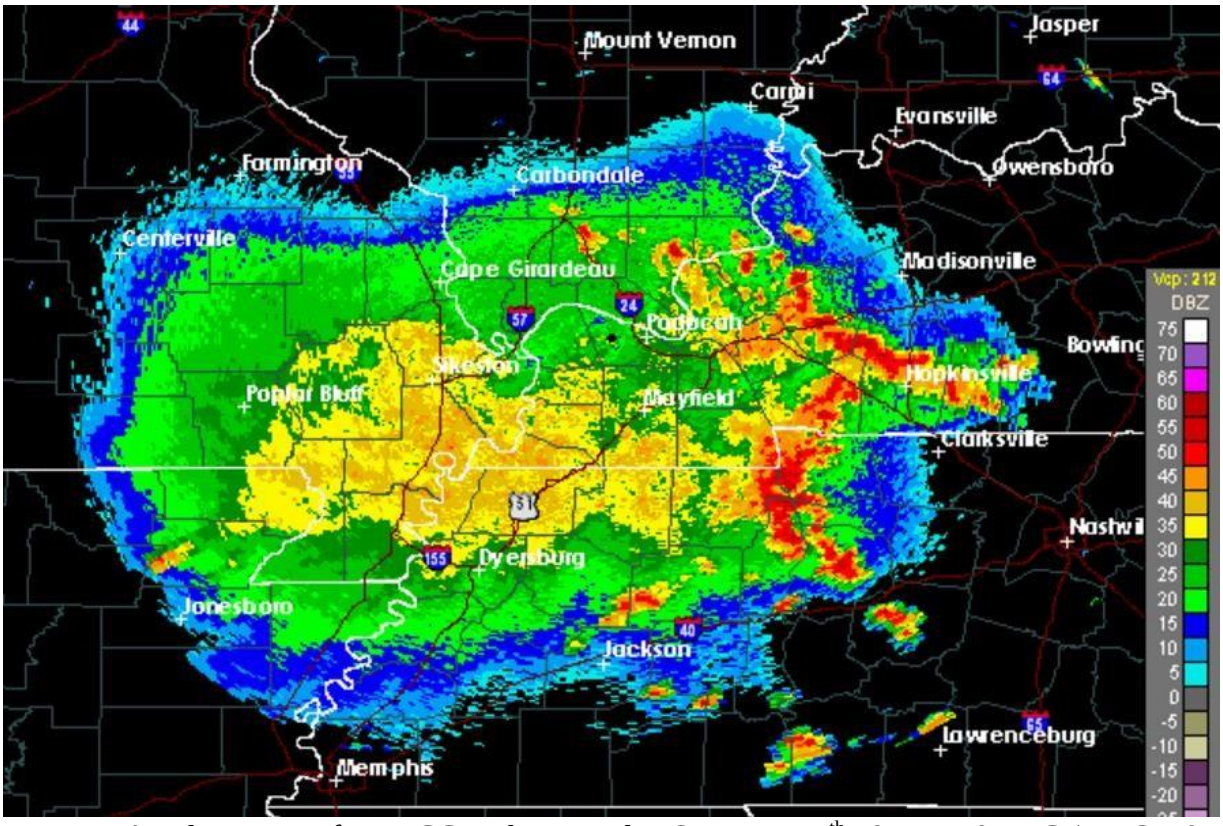

Figure 2.1: A radar image of an MCC in the central U.S. on June 5th 2014 at 20 UTC (NWS, 2014).

2.3 Diurnal Cycle of Precipitation

The diurnal precipitation cycle can vary based on the ocean, land, and orographic conditions. Thus, many places in the world have studied this topic. In the tropics, the diurnal cycle of observed rainfall peaks around 0300 LST, while in the mid-latitude areas, the peak precipitation time is around 0600 LST (Hamilton 1981). Nesbitt and Zipser (2003) also studied the tropical precipitation diurnal cycle using the Tropical Rainfall Measuring Mission (TRMM), finding that rainfall over the ocean has a significant diurnal cycle that peaks in the early morning to predawn hours, with a minimum in the late afternoon. The authors determined that the rainfall maximum is due to rainfall contributions from MCSs.

The diurnal cycle of precipitation has also been studied over contiguous China, showing a significant variation in summer by Yu et al. (2007). Here, the authors studied this cycle in five different regions of China in summer and found that southern and northeast China have late afternoon precipitation peaks due to instability from surface solar heating. The authors also found another

maximum in precipitation during midnight for areas near the Yangtze river at 30 ºN and the eastern portion of the Tibetan Plateau, which is due to the complex terrain in this area (Yu et al. 2007).

The propagation of convective storms across the U.S. has been studied widely as well. Over continental landmasses, the diurnal precipitation cycle has a maximum frequency occurring in the afternoon boundary layer (Dai 2001). MCS's formation is dependent on the outflow from mountain convection (Tucker and Crook 1999). Liang et al. (2004) also studied the diurnal cycle in the U.S., finding the peak of the diurnal cycle occurs at 18 to 21 UTC (Coordinated Universal Time). This cycle begins in spring and continues throughout the summer. This summertime precipitation occurs most frequently in the overnight hours and early morning (Dai et al. 1999), while during other seasons, the diurnal cycle of precipitation is much weaker.

Numerical models are helpful to learn more about how the diurnal cycle sets up storm life cycles. However, in most models, the processes modulating the diurnal cycle, such as surface-atmosphere exchanges, convection, and cloud–radiation interactions are parameterized. Therefore, the capacity to simulate the diurnal cycle proves how effective the physical parameterization schemes are (Bechtold et al. 2004). For example, if rainfall occurs too early after sunrise, the response of the convective parameterization to the diurnal cycle from surface fluxes being too fast, indicating a weakness in triggering convection.

2.4 U.S. Great Plains Convection

As noted previously, spring and summer severe weather in the central U.S. can occur frequently. Thunderstorms impact this part of the country considerably, and as a result, many studies have been done to understand the processes that produce these severe storms. Due to the nocturnal maximum of MCSs in the central U.S., the occurrence of nocturnal storms in this area has been of great interest and studied widely. These studies discovered that this precipitation is crucial to the central U.S. agriculture production and other societal uses such as drinking water and recreation (IPPC AR5 2014).

The PECAN (Plains Elevated Convection At Night) field studies used an array of lower-tropospheric profiling systems, mobile radars, station observations, and aircraft over the Great Plains from June–July of 2015 in order to identify and learn more about nocturnal MCSs and their relationship between the stable boundary layer, low-level jet (LLJ), and atmospheric undular bores. These field studies investigated three mechanisms that are thought to assist in MCS propagation in

the central U.S. (Geerts et al. 2017). These processes include vertical motion from potential vorticity generated by the Rocky Mountains, warm, buoyant air transported from the nocturnal southerly LLJ, and the formation of cold pools and the subsequent undular bores from a passing boundary.

Several papers from this campaign have gone through publishing. For example, Reif and Bluestein (2017) investigated the climatology of convection initiation events at night over the USGP from 1996 to 2015 during April–July. The authors specifically studied storm type, linear system orientation, initiation time, and location, among other characteristics. Composite radar data was used to examine any nocturnal convective initiation with surface data to identify the initiation location of any surface boundaries (fronts, dry line, outflow). The study found that most of the convective events observed began near or on the cold side of the surface boundary.

Stelten and Gallus (2017) also examined nocturnal elevated convective initiation, but with events that occur without direct influence from surface boundaries or pre-existing convection. The authors classified the storm events into four types based on formation and location, then a climatology of each type was performed. The authors conclude that the timing of initiation had one major peak occurring near 04 (23 LST) UTC, with an additional, yet less prominent, peak occurring during 07–08 UTC (02–03 LST).

Modeling has also been utilized to understand these processes better. Bodine and Rasmussen (2017) studied an MCS event in South Dakota on July 6th, 2015, researching organizational changes and periods of rapid forward propagation. The study also uses a high-resolution WRF model for comparison. The authors found that the simulation had good agreement with the observed radar for both events, with confidence that the microphysical scheme (Thompson et al. 2004) in WRF represented the observed processes well.

Many of these studies were done to understand better how and why MCS initiation and propagation occurs leeward of the Rocky Mountains nocturnally. The PECAN overview paper (Geerts et al. 2017) proposes that convection over this region has its origin over the mountainous terrain, acting as an elevated heat source. Convectively generated tropospheric gravity waves develop over the Rocky Mountains and propagate eastward, triggering nocturnal convective systems over the plains.

Furthermore, the LLJ also plays a vital part in nocturnal convection. Occurring most frequently in Kansas and Oklahoma (Song et al. 2005), the LLJ forms nocturnally as the temperature gradient between the Rocky Mountains and the coast of the Gulf of Mexico increases (Ting and Wang 2005). This temperature gradient creates the LLJ, and by morning, the temperature gradient is at its

highest when the continental air mass has cooled off overnight. As a result of the isobaric temperature gradient in the Great Plains, the thermal wind forcing is a critical mechanism that climatologically sets up the LLJ during summer in this area (Parish and Oolman 2010).

As stated before, the LLJ forms nocturnally as the temperature gradient between the Rocky Mountains and the coast of the Gulf of Mexico increases, creating this thermal wind. (Trier et al. 2010). The LLJ can strengthen a cold front, and more importantly, transport moisture to the USGP (Song et al. 2005). The model may have difficulty in producing these environmental criteria for producing nocturnal convection. Conversely, the model overestimates reflectivity and precipitation frequency in the late afternoon and early evening.

2.5 Regional Climate models

Numerical weather prediction is used to predict the short-term state of the atmosphere. However, turbulent flow in the atmosphere and model governing equation assumptions significantly limit predictability beyond a single week, and especially on seasonal and annual time scales. Regional climate models (RCMs) attempt to simulate the climate systems of areas on the order of thousands of square kilometers to entire continents. RCMs are designed to increase their accuracy for more extended time scales. A method to improve this accuracy is to modify various physical parameters in the model. Giorgi (1989) found that adopting a radiative transfer scheme and a land surface model from a global climate model (GCM) improved the energy and water budgets, in turn, making the RCM more accurate in the long term.

Another method to improve climate models is to use a coupled atmosphere and ocean model. Atmosphere-ocean general circulation models (AOGCMs) have been found to improve RCMs by providing boundary conditions (Mearns et al. 2012). This study used four different AOGCMs to provide sea surface temperatures and sea ice boundaries. The study concludes that the RCMs performed well in simulating the mean temperature and precipitation.

RCMs also use either statistical or dynamical downscaled GCMs as a technique to improve accuracy. Statistical downscaling uses statistical relationships between large scale climate variables and local-scale climate responses. Dynamical downscaling uses high-resolution simulations to derive broad-scale climate processes on a local scale (Rummukainen 2010). The main benefit of downscaling is allowing for an increase in resolution without the increase in computational cost.

An additional technique climate models use to improve accuracy is spectral nudging. Spectral

nudging is a procedure that forces the RCM to reproduce large scale atmospheric conditions. The use of nudging has been studied and found to be more accurate by Winterfeldt and Weisse (2009). However, nudging does have its disadvantages such as extreme precipitation events and local scale dynamics, which are not well simulated. The quality of RCMs is heavily dependent on the initial and boundary conditions of the model. A method to improve RCMs boundary conditions is to use hindcasts. Hindcasts use boundary conditions derived from meteorological reanalysis data obtained from observations or general circulation models to recreate the state of the atmosphere. Hindcasts can be a useful tool to test a model's accuracy in reproducing a past event (e.g., Backtesting).

2.6 Convective-permitting climate simulations

Convective-permitting climate simulations (CPCS) are climate models that have a horizontal resolution of, at most, 4-km. Studies have found that CPCS are better at representing convective precipitation as well as the diurnal cycle of precipitation than other climate simulations. Due to most climate models having a horizontal grid resolution between 10 to 100 km, the parameterization of convection becomes a primary source of error in many models (Fosser et al. 2014). In a study done by Kendon et al. (2016), the authors found that due to the finer resolution of CPCS, they are better at resolving orography and the different land surface types, which, in turn, can help simulate convection.

Although CPCSs can resolve convection explicitly, these models must use other parameterizations for atmospheric processes that are much smaller than the grid-scale. These processes include microphysics, radiative transfer (long and short wave), and processes in the planetary boundary layer and on the land surface. Cloud physic processes take place over an extensive range of spatial scales, from microphysics of condensation and evaporation in cloud droplets to the formation of cumulus clouds that are made up from these droplets (Jacob and Miller 2003). Parameterization schemes attempt to simplify these complex processes by using empirical relationships and approximations to model them internally. Parameterization saves computational costs that would require the model to have a much finer resolution.

Additionally, a benefit of high-resolution modeling is an improved representation of boundary layer processes through increased accuracy of land surface orography (Ban et al. 2014). The diurnal cycle of precipitation starts over the Rocky Mountains (orography), then as thunderstorms propagate eastward, the timing of the storms produces a diurnal cycle. With increased resolution, a more accurate simulation of convective storms with regards to the summertime diurnal cycle is possible

(Prein et al. 2015).

However, a limitation to most CPCS's is that no matter the resolution (fine or coarse), temperature biases often result. Studies have shown that although orography and land-surface models show improvement in high-resolution simulations, warm and cold biases still occur (Prein et al. 2013, Brisson et al. 2016). A reason for this is thought to be from cloud-radiation parameterization errors, and also to biases in simulating the central U.S. precipitation diurnal cycle, specifically nocturnal convection (Kraus 1963, Gray and Jacobson 1977, and Sui et al. 1998). These studies confirmed that nocturnal rainfall is related to differential radiative heating between cloudy regions and clear regions, which causes low-level convergence and upper-level divergence to increase during the night and decrease during the day.

2.7 WRF Model Comparison and Validation

High-resolution WRF models are also used to improve forecasting. Located in Norman, Oklahoma, the Storm Prediction Center (SPC) in the US is the center for severe convective weather prediction. To better their forecasting skills, a study done by SPC and the National Severe Storms Laboratory (NSSL) used three different WRF models. They designed and ran high-resolution models to help improve forecasts, then compared their severe storm predictions to forecasts that did not use the help of these high-resolution models (Kain et al. 2006). With no surprise, the study concludes that the WRF models used provided many benefits to the forecasts, with the most robust WRF model earning the best performance regarding convective initiation, evolution, and mode.

The validity of the temperature and precipitation of the WRF model used in this research has been briefly studied by Liu et al. (2016). This study discovered that the model has a deficiency in summer precipitation. There is a low bias of thunderstorms in the central U.S., indicating that the propagation convection leeward of the Rockies is too weak. In a study done by Prein et al. (2017a) the authors use a feature tracking algorithm to compare this model's precipitation output to a radar-based and observation-based precipitation product (Stage IV). This study uses the same model used in the study also. The authors found that the model was able to produce propagating convection across the U.S., but MCS frequency underestimation did occur in the Central U.S. during the late summer months.

While the most significant biases in this model's results are in the frequency of MCS's produced, the ability for the model to realistically produce propagating convection is a huge step

forward in regional climate simulation. Realistic storm propagation is due to the model's fine horizontal grid spacing in order to turn off convective parameterization and allow the model to simulate deep convection explicitly. One of the main objectives of climate simulations is to model the current state of the climate realistically. Thus, in order to judge a model on its correctness, one must validate it against a set of observational data that the model was trying to simulate, an aspect this research will take.

In Gutowski et al. (2003), the authors use the Regional Climate Model system RegCM with a horizontal resolution of 52 km. The study concludes that the simulated precipitation intensities are underestimated compared to the observation data. Here, authors examined precipitation intensities over 6, 24, and 240 hour totals. The study found that, for warm-season precipitation and all hourly totals, the model and observations were significantly similar for lower intense precipitation rates, however, the model underestimated the frequency of more intense rates. Another observation experiment and model comparison comes from the International H2O Project (IHOP_2002). This study found that gust fronts and surface convergence play a role in convective initiation. Also, although the model was able to forecast 44% of the studied initiation episodes correctly, the forecast accuracy is dependent on the scale of the initiation mechanism (i.e., frontal boundary, cold pool, outflow) (Wilson and Roberts 2006).

A limitation to using radar data with precipitation validation is that radar rainfall estimates contain regular errors in rainfall detection. Of these errors, most include the radar beam missing a large portion of the storm (LaDue et al. 2010). Moreover, a limitation to using station observations in precipitation validation comes from a sparse network of stations as well as outliers, inhomogeneities, missing data, spatial and temporal sampling problems, and instrument bias (Karl et al. 1993, Guttman and Baker 1996).

2.8 Climate Change Impact Assessment

Earth, its atmosphere, and ocean all play a role in weather and climate. The atmosphere is directly impacted by incoming solar radiation through reflection and absorption of the atmosphere, clouds, and Earth. A major unknown in the Earth’s climate system is the future of greenhouse gas concentrations in the atmosphere and how the climate system will react to these conditions. Global climate change can influence many processes on Earth.

Arguably, one of the more notable changes that are occurring as a result of global climate

change is sea-level rise. Since much of Earth's population lives next to the ocean, they are in danger from this threat. Sea-level rise is partially caused by a global mean surface temperature rise, causing thermal expansion and glacial, and sea ice amount to decrease. Creating a feedback loop, this decrease in sea ice causes the surface albedo (sunlight absorption/reflection) to rise, increasing the surface temperature, leading to more sea ice melt. This feedback has been named the ice-albedo feedback loop. The increase of CO_2 and other greenhouse gases can strengthen the ice-albedo feedback through the greenhouse effect, enhancing the effects of sea-level rise, global mean surface temperature increase, and causing ice cap amounts to decrease (Karl and Trenberth 2003).

The aerosol effect can also have an impact on climate change. Aerosols are small solid or liquid particles in the atmosphere that help the formation of cloud droplets and rain. However, an increase in the concentration of aerosols can produce more, smaller condensation nuclei, which will cause precipitation in the form of drizzle, rather than rain. This process then increases cloud height and lifetime, which causes a net warming effect on the atmosphere. (Ramanathan et al. 2001).

The IPCC 5th assessment reports that it is 'very likely' heatwaves frequency will increase and last longer, and extreme precipitation events intensity and frequency will increase in many regions. For example, Figure 2.2 depicts how an increase in the mean and variance of temperature can produce more extreme warm weather. In a study done by Allen and Soden (2008), the natural climate variability was used to demonstrate a direct link between a warmer climate and an increase in extreme precipitation frequency using both satellite observations and model simulations.

The Clausius-Clapeyron equation describes how the vapor pressure varies as a function of dewpoint temperature and how the saturation vapor pressure varies with respect to air temperature. Due to this relation, there is a correlation between the increase in extreme surface temperature and extreme precipitation events. As temperature increases, the saturation vapor pressure also increases due to the amount of water vapor in the saturated air increasing, which implies that warm air can contain more water vapor than cold air. Thus, warm air storms can produce much more rain. In a study done by Pall et al. (2006), for mid/high latitudes, the observed increase in spatial mean precipitation frequencies agreed with the Clausius-Clapeyron predicted increase. This finding was also found to be consistent with other climate model forecasts and indicates that regions, where the surrounding flow changes the least in the midlatitudes, shows the most considerable agreement with Clausius-Clapeyron projected change.

Moreover, the increase of CO_2 amplifies this feedback by increasing the greenhouse effect, creating positive feedback by allowing the air to retain more water vapor, and so on (Hartmann 2015).

Climate models have also been used to study the possible increase in heavy precipitation. For example, an RCM for Europe found that with a 2° Celsius increase in surface temperature leads to a 20% increase in precipitation events more significant than 30 mm hr^{-1} (Frei et al. 1998), while another study found that precipitation frequency can increase by 40% per 1 ºC of warming in the tropics (Chou et al. 2012). The authors note that this response is also higher for maritime regions.

In the western part of the USGP is the Ogallala Aquifer. This aquifer is essential to agriculture in this part of the U.S. due to the demand for irrigation. The aquifer is replenished from snowpack drainage off the Rockies in spring and propagating precipitation systems that form leeward of the Rockies in summer (Rosenberg et al. 1999). In the future, the need to produce more crops to sustain the population will increase due to the rising population of humans. A decrease in precipitation and depleted irrigation sources could impact agriculture and shift growing areas to the north as precipitation is the leading source of aquifer recharge (McGuire 2017, Moore and Rojstaczer 2002).

This shift in growing areas and escalation in human population poses additional challenges in producing food and other health impacts. A WRF simulation study in the high USGP simulated precipitation indicated that the semiarid climate in this area would experience an increase in drought with climate change (Harding and Snyder 2014). The authors of this study also propose more research be done on the sea surface temperatures in the future as the impact of this will affect the moisture transport in the LLJ which is mainly responsible for the frequency and intensity of precipitation in this part of the country.

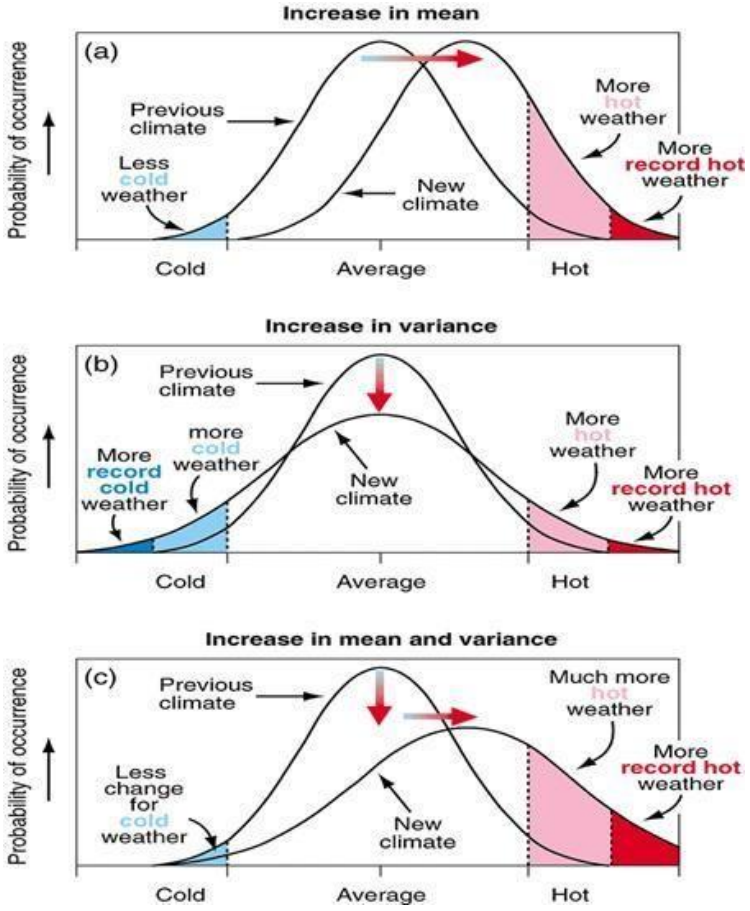

Figure 2.2: How an increase in mean and/or variance of temperature will impact the probability of occurrence of hot and cold extreme weather (IPCC AR5 2014).

2.9 Pseudo Global Warming Method

As noted previously, greenhouse gas concentrations continue to increase in the atmosphere, and the effects of climate change are beginning already. With threats on the crop production (Watson et al. 1998) and economic loss from the increasing frequency of severe storms (IPCC AR5 2014), it is vital to understand how a possible future climate will impact thunderstorms.

One procedure that attempts to project the approximate future climate is called the Pseudo Global Warming method. The use of the PGW method was implemented into a model by Schär et al. (1996). The authors performed a historical simulation forced by the European Centre for Medium-Range Weather Forecasts (ECMWF) and a PGW run that placed a constant increase of +2 Kelvin in the atmosphere, land-surface, and sea-surface temperatures, yet keeping the relative humidity unchanged. This PGW method was described as sufficient, finding the mesoscale atmospheric

feedback from increased moisture content and the radiative effects of changes in cloud cover and water vapor to be advantageous in ensuring the accuracy of large scale flow in the simulation.

In another experiment, Kawase et al. (2009) also used multiple models to investigate the Baiu rainbands in southeast Asia from the 1990s. In this study, the authors used a WRF model forced by ERA40 (ECMWF Re-Analysis) data for the historical simulation and the PGW data using the SRES-A1B (Special Report on Emissions Scenarios) to simulate the future (2060–2089) climate, keeping the variability of short-term disturbances and interannual variability to be similar to that in the 1990s. This study states that, though this PGW method neglects the changes in interannual climate variability, the PGW downscaling method assess changes in regional climate responses due to GHG emission increases.

In a similar methodology used for the PGW method in this study, Rasmussen et al. (2011) ran a retrospective and PGW model to study the hydrological cycle in the Colorado Headwaters region of the Rocky Mountains. Here, the authors used a WRF model for both the historical and PGW simulations. The PGW approach taken used a future (2045–2055) monthly 10-year climatology subtracted from a current (1995–2005) monthly 10-year climatology, to produce a monthly climate perturbation signal. This study concluded that the PGW experiments show a consistent increase in precipitation on the order of 10%–15% in a future climate over the Colorado Headwaters region. This research is consistent with findings from Allan and Soden (2008), which found that low-level moisture will rise with the temperature at about 7% per Kelvin, supported by the Clausius-Clapeyron equation.

2.10 Literature Review Summary

MCSs are frequent in the central US during spring and summer, and are a major contributor to precipitation in this area. These storms can also be severe, causing costly damage to society and infrastructure. Thus, these storms have been researched for decades and there has been much interest in using NWP to simulate and further study the mechanisms that cause severe storms in the central US. Convection-permitting NWP models simulate convective processes more realistically than coarser grid models due to errors in local-scale processes and convective parameterization not accurately producing convection.

Modeling nocturnal propagating convection in the central U.S. has been a longstanding difficulty in the model research community. With the use of convective permitting simulations, this

model deficiency has been improved. This is due to the improvement of the land surface schemes and boundary layer processes that have shown to be more accurate with finer horizontal resolution. Yet, some model biases still occur, mainly due to the parameterization of more complex processes that are difficult to explicitly simulate.

Moreover, there is also a large interest in learning how the characteristics of precipitation systems in the central US will be impacted by climate change. Due to greenhouse gas concentrations continuing to increase in the atmosphere, efforts have been made to use Pseudo Global Warming techniques in NWP to project future climate scenarios. This study will take these issues into account while examining the model simulation to analyze the accuracy of the historical simulation and learn how and why propagating convective systems will change in the future climate projection.

Chapter 3. Materials and Methodology

This section discusses the data analyzed in this study, including the WRF simulation in two parts, and the observational data. This study presents a validation of the WRF simulated composite (column maximum) radar by the Weather Surveillance Radar-1988 Dopplers (WSR-88Ds) national mosaic. Along with radar data, the hourly accumulated simulated precipitation is validated against the Stage IV multisensory gridded observed precipitation product.

Simulation (CTRL and PGW) and observation hourly data is analyzed by season (March, April, May, and June, July, August), as well as by intensity (threshold >40 dBZ and >10 $mmhr^{-1}$). The histogram and diurnal cycle evaluation is analysis domain wide while the statistical testing and hovmöller analysis is broken down into three sub regions. The Wilcoxon Rank sum test is used between the observation and simulation data (OBS and CTRL) and both simulation (CTRL and PGW) to compare the distributions of data with a 95% confidence interval. The historical simulation and PGW simulation are also compared in regard to histogram, diurnal cycle, and hovmöller diagrams. Further detail of the methodology and data used in this analysis is as follows.

3.1 WRF Simulation

This research project uses the simulations performed using the Advanced Research Weather Research and Forecasting (WRF-ARW) model version 3.4.1 (Skamarock and Klemp, 2008) over the entire continental U.S. on a convection-permitting configuration (Liu et al. 2017). Two parts compose these model simulations: (1) A 13-year (2000–2013) simulation of historical weather and climate patterns, and (2) A pseudo global warming (PGW) simulation to project the weather and climate at the end of the 21st century. The historical (CTRL) 13-year simulation was designed to have 4-km grid spacing covering the entire continental U.S. and the southern portion of Canada (up to 56 ^{o}N) with a domain size of 1360 by 1016 grid points (5440 km East/West and 4064 km North/South). The vertical extent of the model covers 51 stretched levels reaching up to 50 hPa.

The main physical parameterizations used to set up the model include: Thompson and Eidhammer (2014) microphysics scheme, Noah Multi-Physics Land-surface model (Niu et al. 2011), Yonsei University planetary boundary layer (YSU, Hong et al. 2006), with the Rapid Radiative Transfer Model (RRTMG, Iacono et al. 2008) used for both long and short-wave radiation.

This model uses the 6 hourly 0.7-degree ERA-Interim reanalysis (Dee et al. 2011) for forcing initial and boundary conditions. The 75-km lateral grid spacing from ERA-interim uses dynamical downscaling to the 4-km WRF grid. Spectral nudging was also utilized in the model to keep boundary conditions within statistically normal ranges at each grid point. Variables that the spectral nudging used are air temperature, geopotential, and the horizontal wind above the PBL to more accurately simulate large scale atmospheric conditions.

This convection-permitting, sizeable geographical extent, and long-term WRF regional climate simulation enable an improved representation of atmospheric processes. Downscaling to a higher resolution permits the model to simulate deep convection without parameterization. Therefore, it is essential to assess the model in terms of its convection producing capabilities. More detail of the model set up, and performance can be found in Liu et al. (2016).

Model version	WRF V3.4.1
Domain	19–57°N, 139–56°W, From 140 m below the ground to up to 50 hPa (~ 20,000 m ASL)
Main input variables	Soil and air temperature, wind speed, soil moisture, atmospheric pressure, Relative Humidity
Spin up period	3 Months
Initial and lateral boundary conditions	ERA-Interim Reanalysis
Physics:	
Microphysics	Thompson and Eidhammer
Land surface	Noah MP Land Surface
Planetary Boundary Layer	YSU (Yonsei University)
Convective parameterization	None
Long wave/Short wave radiation	RRTMG

Table 3.1: WRF model specifications (Liu et al. 2016).

In addition to the WRF historical (CTRL) simulation, the Pseudo Global Warming (PGW) method is a supplement to the CTRL simulation that uses data from the RCP (Representative Concentration Pathways) 8.5 scenario. The RCP 8.5 greenhouse gas emission scenario is a high emission 'business as usual' scenario that projects a 3.7° Celsius global mean temperature increase by the end of the 21st century.

The 30-year CMIP5 (Coupled Model Intercomparison Project) 19 model ensemble monthly mean using calculations between the change of the historical period 1976–2005 and future period, 2071–2100 RCP 8.5 scenarios. First, calculations are done to find the mean changes in temperature, U and V wind, geopotential height, specific humidity. Next, the calculated change is added to the ERA-Interim, forcing data to rerun the model. The PGW simulation uses the same 6 hourly ERA-Interim data; thus, the weather reanalysis data is the same. The following shows how the WRF model, ERA-Interim, and CMIP5 are used to calculate the climate perturbation:

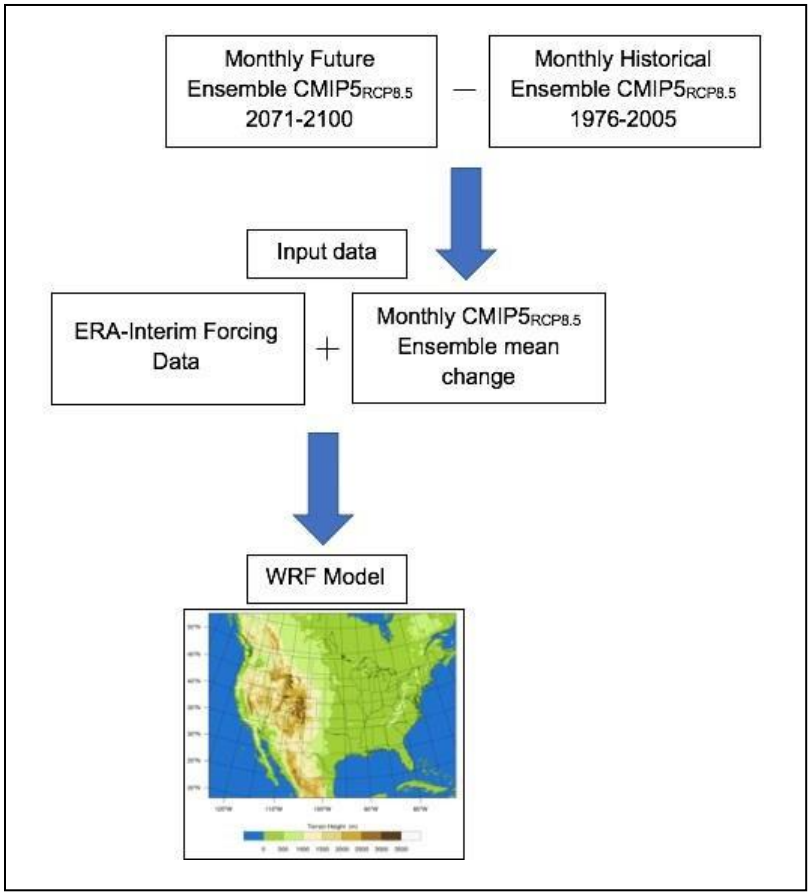

Figure 3.1: Flowchart showing how the CMIP5 and ERA-Interim data is used in the WRF simulation. (Liu et al. 2016).

$$WRF_{input} = \text{ERA-Interim} + \Delta CMIP5_{RCP8.5} \quad (3.1)$$

$$\text{Where } \Delta CMIP5_{RCP8.5} = CMIP5_{2071–2100} - CMIP5_{1976–2005}$$

3.2 Observation Data

The observed radar data comes from the National Weather Service (NWS) national array of radars, with post-processing performed by the NSSL. The United States has a system of weather radars called Weather Surveillance Radars-1988 Doppler (WSR-88Ds) or Next Generation Weather Radar (NEXRAD). The NEXRAD network is made up of 159 high-resolution S-Band Doppler weather radars operated by the NWS. This data is available for download. Inside our analysis domain, there are roughly 25 of these radars. This data has been collected and archived by NSSL, who then mosaics images together for each radar site and processes the data into a national composite set of imagery.

The observed precipitation data comes from the Stage IV dataset. This product uses both surface radar and station precipitation measurements to create a gridded hourly precipitation dataset for the CONtiguous United States (CONUS). Stage IV is a product from the National Centers for Environmental Prediction (NCEP). Current Stage IV analysis data is available from the NCAR RDA at: https://doi.org/10.5065/D69Z93M3.

NCEP uses radar data to estimate precipitation amounts using an MPE (Multi-sensor Precipitation Estimator) algorithm and station precipitation data to quality control and process the data (Nelson et al. 2010). Based on the location of the data in the U.S., the radar precipitation estimating algorithm uses the Hydrologic Rainfall Analysis Projection (HRAP) grid. After the radar data is processed, the images are then mosaicked to create a gridded, 4-kilometer resolution hourly precipitation analysis for CONUS.

3.3 Analysis domains

The analysis domain area of focus for comparing the models is over the central U.S. From the eastern edge of the Rocky Mountains to the western boundary of the Mississippi River states. The

analysis domain is inside the latitudes 30–45 ºN, and the longitudes 90 ºW–105 ºW. In this area, convective precipitation plays an essential role in supplying the central United States with water resources that are crucial to the area.

West of the analysis domain is the Rocky Mountains, which is where most storms come from or form just leeward of the Rockies (Feng 2016, Fritsch et al. 1986). In this area, throughout spring and summer, an upper-level trough will propagate eastward across the western U.S., providing a source of storm initiation leeward of the Rocky Mountains. Later in the summer, more storms begin to form in the northern Great Plains and southern plains of Canada. The northern portion of the analysis domain extends to the northern US and southern Canada where MCS frequency begins to decrease.

Subtropical Texas and the Gulf of Mexico is south of the analysis domain, where precipitation is more tropical (Kunkel et al. 2010). Extending East of the analysis domains is the eastern plains, Appalachia, and the subtropical Southeastern U.S. In this part of the country, storms form in March and April, especially in the southeastern U.S. In the area northeast of the analysis domain we would see some lake effect precipitation signals due to the Great Lakes, although this would only be at the end of the lake effect snow season, which concludes in March.

The propagation of storms that occur in the analysis domain account for about 60% of the total warm-season precipitation (Carbone 2008) for the central U.S. Carbone 2008 also showed that the western portion of the Mississippi River valley is where many MCSs begin to dissipate. Furthermore, precipitation events (daily totals above 12.7 mm) contribute to roughly 70% of the annual precipitation in the central U.S. throughout nearly 25% of all rainy days (Groisman 2012). Extreme events are essential to study to understand how the future trend of precipitation events in the central U.S. change under a pseudo global warming scenario.

For the hovmöller investigation, we divide the analysis domain into three different regions of 5-degree latitude bands, 30 ºN–35 ºN (R1), 35 ºN–40 ºN (R2) and 40 ºN–45 ºN (R3). Subsections are used to observe the different storm propagation patterns that occur in these areas. For example, in R1, the warm season diurnal cycle begins earlier than in R3, due to R3 being more North and therefore colder at the same point in the season.

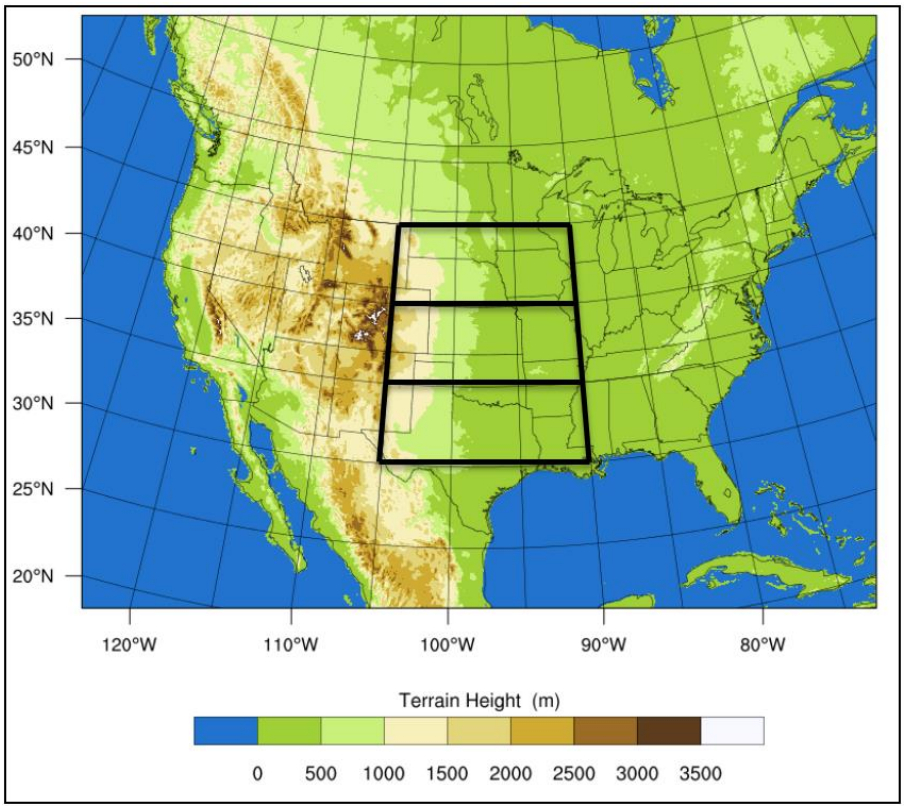

Figure 3.2: The WRF model domain and analysis domains (black).

3.4 Statistical Analysis

As a test of significant similarity or difference between two distributions, we use the non-parametric Wilcoxon rank-sum test. Assuming a non-normal distribution, this test is used to assess a statistically significant comparison between the WRF CTRL simulation and observations, and between WRF CTRL and WRF PGW. This test will be performed for both reflectivity and precipitation distributions, including a stratiform and convection analysis. Using alpha [α] as 0.05 for the confidence interval, this allows us to determine how the two datasets compare given a 95% confidence level.

To begin the test, let x and y be two random, independent samples of size m and n. The Wilcoxon rank sum statistic is the number of all pairs (x_i, y_j) for which y_j is not greater than x_i. Then arrange the $n_1 + n_2$ observations of the combined sample in ascending order, assigning ranks from the smallest value to the largest value. Next, calculate w_1 , the sum of the ranks of n_1 from the samples:

$$w_1 = \frac{(n_1 + n_2)(n_1 + n_2 + 1)}{2} - w_2 \qquad (3.2)$$

Then calculate u_1 using the following equation:

$$u_1 = w_1 - \frac{n_1(n_1+1)}{2} \qquad (3.3)$$

We use a two-tailed test to determine the relationship between the two datasets on both sides of the distribution. The null hypothesis, H_0, is rejected in favor of the alternate hypothesis, H_1, if the calculated P-value is smaller than α, the confidence level. If we accept H_0 then $\tilde{\mu}_1 = \tilde{\mu}_2$ and accept H_1 if $\tilde{\mu}_1 \neq \tilde{\mu}_2$ where $\tilde{\mu}_1$ and $\tilde{\mu}_2$ are the data distributions. By calculating the P-values for the Wilcoxon rank sum test, differences between two distributions can be represented with a given confidence (Walpole 2012).

Another statistical display of data used in this study is box plots, used to show the spread of the data, and are a visual representation to show four distinct quartiles of data. The first quartile (Q1) shows the lowest quarter of the data, the second quartile (Q2) is the next highest, and so on from the third quartile (Q3) through the fourth quartile (Q4) showing the highest quarter spread of data. The shape of the box plot shows the minimum quartile (Q1) as a 'whisker' extending to the bottom box, which is Q2. Q3 is the next box, and finally, Q4 is the top whisker extending from the Q3 box. It is essential in statistical analysis to understand that the limitation of this study is that the statistical analysis of climate data cannot prove the physical causes of any changes in extreme precipitation events.

The statistical test using a variable correlation coefficient (CC) is also utilized. The Pearson CC is a single value calculated from two variables by finding the covariance divided by the product of their standard deviations. It is a normalized measurement of how the two are linearly related. The hovmöller correlation is computed using a pattern correlation function on a centered grid. This statistic can be computed between two variables for their locations on two different maps. The CC r_{xy} is calculated by the equation:

$$r_{xy} = \frac{1}{n-1}\sum_{i-1}^{n}\left(\frac{x_i - \bar{x}}{s_x}\right)\left(\frac{y_i - \bar{y}}{s_y}\right) \qquad (3.4)$$

Where

$$s_x = \sqrt{\frac{1}{n-1}\sum_{i=1}^{n}(x_i - \bar{x})^2}$$

$$s_y = \sqrt{\frac{1}{n-1}\sum_{i=1}^{n}(y_i - \bar{y})^2}$$

3.5 Reflectivity Population Distribution

As a radar transmitter sends out microwaves, it can identify precipitation falling in the sky by detecting targets (i.e., rain or snow) in the atmosphere from the echoes reflected to the radar receiver. The computer displays the echoes as an image (Figure 2.1) that the radar processes to its display. The units of measurement computed from the power measurement taken by radar to produce an image are dBZ, decibels of the radar reflectivity factor Z. For smaller dBZ values, there are fewer hydrometeors scanned by the radar, and vice versa (higher dBZ, more precipitation). Figure 3.3 shows different levels of dBZ that correspond to rainfall rates and precipitation intensities.

There are two main types of radar reflectivity data. One is base reflectivity, which shows the reflected energy for a single scanned elevation angle, which is most often the lowest, or 'base' level. The other is composite reflectivity, which shows the maximum data point for all scanned elevation angles. This study will compare the WRF simulated composite radar to the observed radar by computing and plotting the probability distribution function of this data, including an investigation of the different reflectivity bins with increasing intensity. Note Figure 3.3, here we see the different levels of reflectivity values and what they represent in terms of precipitation intensity; thus, we can compare the differences in frequency for light (stratiform) and heavy (convective) precipitation.

Figure 3.3 shows the relationship of reflectivity to the precipitation rate using the empirical power-law relationship of the reflectivity factor to rainfall rate conversion using the Marshall Palmer ZR relationship, all of which follow the same basic formula:

(3.5)

$$Z = AR^b$$

For example, the Marshall Palmer stratiform formula

(3.6)

$$Z = 200R^{1.6}$$

(3.7)

A typical ZR relationship used in the NWS developed at NOAA: $Z = 250R^{1.2}$

(3.8)

Summer season with deep convection on radar uses a modified version: $Z = 300R^{1.4}$

where R is the rainfall rate (mm hr^{-1}), Z is the radar reflectivity factor (mm^6/m^3), and A and b are empirical constants (Rinehart 2010). This formula is one of the most commonly used (especially for mid-latitudes) relations to compute rainfall amounts from radar data. For this study, we will describe radar reflectivity and precipitation similarly using this table of related quantities. For low values, we will be referring to reflectivities between 0–25 dBZ and precipitation rates between 0–1.3 mm hr^{-1}. For moderate reflectivity values, we will be referring to 25–40 dBZ, and precipitation rates between 1.3–11.53 mm hr^{-1}. Finally, for heavy reflectivities, vales between 40 and above and precipitation rates above 11.53 mm hr^{-1}.

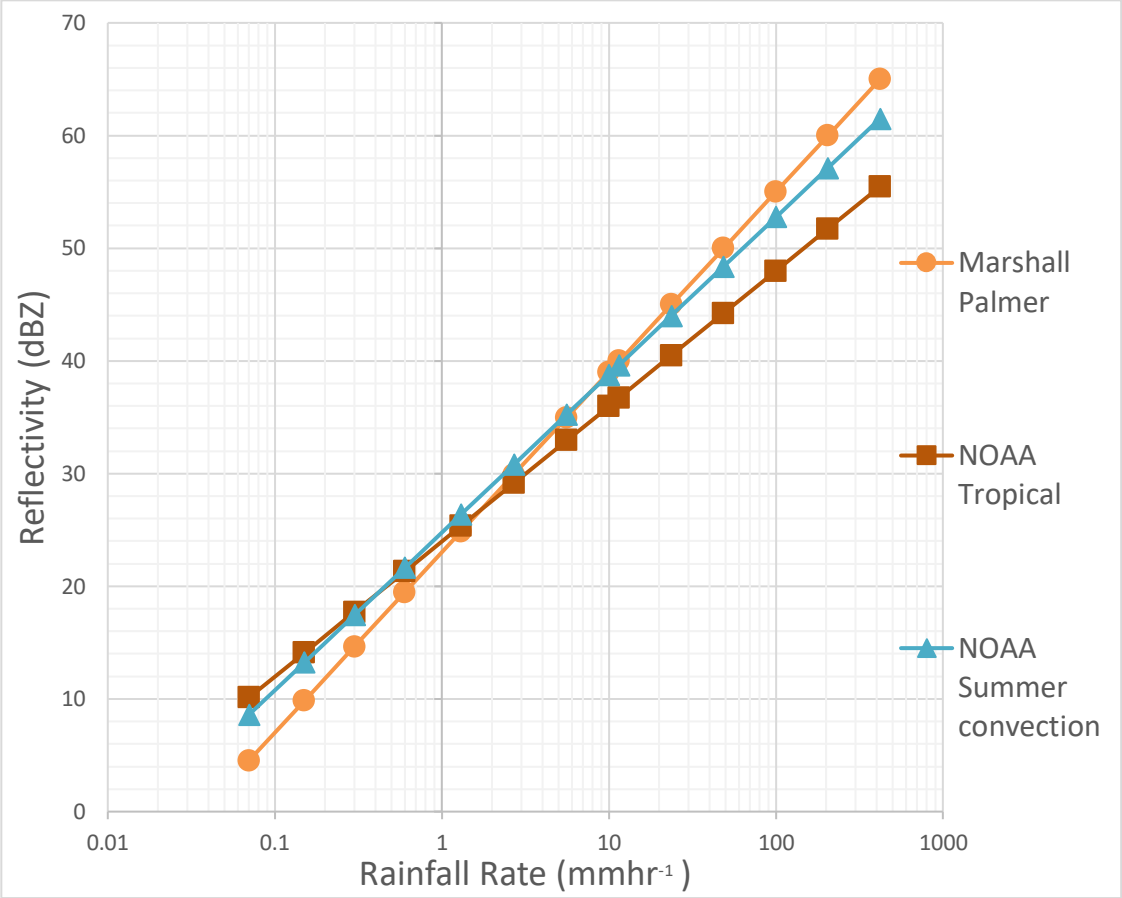

Figure 3.3: A comparison of three different ZR relationships showing how radar reflectivity varies as a function of rainfall rate.

Figure 3.3 shows three ZR relationship formulas. These equations are shown to compare how reflectivity is used to calculate potential rainfall rates used in the observed rain data. In this study, 'light' precipitation will be referred to when discussing 0–20 dBZ or 0–0.5 mm hr^{-1}, 'moderate' precipitation will be referred to when discussing 20–40 dBZ or 0.5–10 mm hr^{-1}, 'heavy' precipitation will be referred to when discussing 40–60 dBZ or 10–50 mm hr^{-1}, and finally 'extreme' precipitation will be referred to when discussing >60 dBZ or >50 mm hr^{-1}.

The 'light,' 'moderate,' and 'heavy' thresholds have been used in a variety of studies to investigate precipitation intensity. Stone et al. 2000 uses 0.6, 2, and 5 mm day^{-1}, which converts to 0.025, 0.083, and 0.2083 mm hr^{-1}. The U.K. Meteorology Office classifies precipitation as 'slight,' 'moderate,' 'heavy,' or 'violent' for rainfall rates from 0–2, 2–10, 10–50, or greater than 50 mm hr^{-1}, respectively. The AMS defines the intensity of rainfall at any given time and place to be classified as "light," for rainfall rates from 0–2.5 mm hr^{-1}, "moderate" rainfall from 2.6–7.6 mm hr^{-1}, and "heavy"

rainfall rates over 7.6 mm hr^{-1}.

This research uses a threshold of reflectivity and precipitation data to separate stratiform precipitation from convective precipitation. For values below 40 dBZ or 10 mm hr^{-1}, we assume to be stratiform precipitation, and above this threshold, we take as convective precipitation. This method, called the Background Exceedance Test (BET), has been widely used in the past. Studies that have used this method of thresholding specific values have found that this method is sufficient in dividing stratiform from convective rain. Houze (1973) first used a BET threshold, and other studies (Steiner et al. 1994 also used 40 dBZ threshold) have also applied this technique to threshold radar (using 40 dBZ threshold) and precipitation (using 5 or 10 mm hr^{-1} thresholds) data. This technique and others classify precipitation as convective when the rain rate exceeds a certain background threshold amount (Lang et al. 2003, Penide et al. 2013, Yang et al. 2013).

3.6 Diurnal Cycle Analysis

By analyzing the model in terms of the hourly data throughout the day, this research analyzes the diurnal precipitation cycle. The precipitation diurnal cycle plots show all reflectivity values, and values above 40 dBZ to investigate convection. For each hour, the frequency of values is found, then the relative frequency is calculated with respect to each variable, and plotted against the time (UTC) for the entire analysis domain.

In addition to analyzing the separation of stratiform from convective precipitation, we investigate the diurnal cycle in two seasons. The seasons analyzed are March, April, and May (MAM) for the spring season, where the diurnal cycle is less pronounced, then June, July, and August (JJA) is the summer season, during which the diurnal cycle is most pronounced diurnal signal due to the increase in solar insolation (Fabry 2012).

Therefore, the focus of this thesis is on the analysis of summertime (JJA) convection in the historical and PGW simulations. In this season, the diurnal cycle spatially varies the most. To measure the variation of the diurnal cycle, we investigate the reflectivity and precipitation data in exploring when and where relative frequency minimums and maximums occur and compare the simulation to observations to analyze the model output.

3.7 Hovmöller Analysis

Due to the diurnal cycle varying in both space and time, investigating the analysis domain as a whole can lead to smoothed and lost data features. To mitigate detail loss, we separate the analysis domain into 5 degree latitude bands. We create hovmöller diagrams for areas ranging from 30 ºN to 35 ºN, 35 ºN to 40 ºN, and 40 ºN to 45 ºN (Figure 3.2). The 5-degree latitude bands were chosen because case studies (Wetzel et al. 1983) and observational climatology studies (Tuttle and Davis 2006) have found that warm-season convection leeward of the Rocky Mountains is frequently confined to 5-degree latitude bands. These storms are also regularly impacted by strong meridional forces such as surface fronts and the LLJ. Studying the analysis domain as a whole also introduces some smoothing and may remove details from the data. By dividing the analysis domain into three latitude bands, we can average across fewer data together and analyze critical details lost in an analysis of domain-wide averaging.

This portion of the study is similar to the diurnal cycle analysis, but a useful method to identify storm propagation characteristics is to create hovmöller diagrams. Hovmöller diagrams are used to compare the WRF model and observed radar spatiotemporally. By plotting the reflectivity values for corresponding time and longitude, we can compare the evolution of storms across the analysis domain over time, highlighting the longitudinal propagation of these storms, and other characteristics such as duration of storms and speed.

The hovmöller diagram is made to show how data features in a particular area vary over time. The first step in making a normalized (relative) frequency hovmöller diagram is to find the frequency of all or convective precipitation to calculate the relative frequency. Then the average of all the relative frequency values by grid box in each band of latitudes and for each similar hour of the day (i.e., 00Z, 01Z, 02Z) is computed so that the calculations are for data taken from similar times of the day. Therefore, we can get an idea of the relative frequency of when and where storms occur and visualize their propagation eastward across the analysis domain.

The frequency of reflectivity and precipitation is analyzed. To do this analysis, we find the frequency of all values in the data for each longitude and similar hour of the day, averaged over latitude. By reducing the data dimension by one (eliminating latitude), this creates time as a function of longitude. This relative frequency is shown as a percent in the hovmöller figures. This plot is beneficial in determining when and where propagation of convection begins in the leeward of the Rockies. In a study done by Carbone and Tuttle (2008), the authors analyzed observed radar data in the central U.S. and found that rainfall was present 65% of the time at 105 ºW during 2100 UTC. This study looks for similar spatiotemporal patterns in convection initiation.

3.8 Future Projection Analysis

This portion of the study aims to compare the historical regional climate model to a pseudo global warming projection to investigate differences between the simulated composite radar and precipitation. The secondary objective of this study is to evaluate the PGW projection to understand how a future climate will impact radar reflectivity distribution, the diurnal cycle of precipitation and storm propagation.

The PGW analysis of this model is similar to the historical (CTRL) model analysis. To achieve the second objective, which is to analyze the change in radar reflectivity distribution and the diurnal cycle of precipitation and storm propagation, this study compares the historical CTRL model to the future PGW projection. Data from the PGW simulation is studied with the purpose to learn how a future projected climate impacts characteristics of stratiform and convective precipitation and how this change impacts the agriculture and infrastructure in the central U.S.

This study investigates the changes in the frequency of extreme precipitation from the historical simulation to the future climate projections. Similar statistical methods (histograms, Wilcoxon, standard deviation) used to investigate these differences. We also explore any significant changes in precipitation intensities and amounts and consider how and why these changes occur in the PGW future climate simulation.

The diurnal cycle of precipitation is also investigated to evaluate the changes in the intensity and timing of convective precipitation. In the future climate, the convective storm characteristics may change due to an acceleration in the hydrological cycle, making convection susceptible to more frequent or/and more intense precipitation. These changes can be evaluated using the hovmöller and histograms for different intensity ranges.

The upper extreme of the reflectivity and precipitation data (>50 dBZ and >50 mm hr^{-1}) is also examined. A focus of this thesis is in determining the change of extreme convective storms from the historical climate to a PGW projection of the future climate. We are interested in seeing how extreme reflectivity and rainfall rates is affected by an increase in greenhouse gas emissions simulated by the WRF PGW model.

Chapter 4. Results

This section presents the results of the investigation of the WRF model's capabilities of simulating warm-season convection in the central United States. This study found that the WRF simulation overproduces the frequency of mist and light precipitation (0–15 dBZ). During MAM and JJA, WRF underestimates the frequency of reflectivity values between 20–40 dBZ. The WRF CTRL model underestimates moderate to extreme precipitation rates. In MAM, WRF CTRL underestimates reflectivity values from 08–14 UTC (nocturnal convection). Similarly, during JJA WRF CTRL diurnal cycle peaks at 23–06 UTC, significantly exceeding the amplitude of the OBS. Hovmöller diagrams show the propagation of storms eastward, and the peak in the simulated late afternoon matches the observations, but WRF CTRL underestimates the frequency values and propagation overnight.

While similar areas of storm propagation between OBS and WRF occur, WRF CTRL overestimates the frequency of reflectivity values in MAM, yet under produces convection in JJA during the day. From the PGW simulation analysis, there is an increase in extreme simulated reflectivity and precipitation rates during MAM and further in JJA compared to WRF CTRL. The organization of the results of this study is by statistical analysis, reflectivity histograms, diurnal cycle analysis, and hovmöller diagrams.

4.1 Statistical Analysis

The simulated reflectivity distribution was found to be significantly different from the observed reflectivity distribution with 95% confidence for both MAM and JJA. This result is shown in Table 4.1, which uses the Wilcoxon Rank Sum test to compare these two distributions as a whole and the stratiform portion of the distribution (values <40 dBZ). More intense reflectivity values often associated with convective precipitation (values >40 dBZ) do pass this test for all three regions in MAM and JJA, meaning that with 95% confidence, the WRF and observations data have similar distributions.

The Wilcoxon test comparing the simulated precipitation to the Stage IV observed precipitation shows similar results as the reflectivity data. Table 4.2 shows the convection (>10 mm hr^{-1}) for both MAM and JJA, is similar with 95% confidence between the WRF CTRL and

observations for all three regions. For all data points and stratiform precipitation rates (<10 mm hr^{-1}) in MAM and JJA, the data reject the null hypothesis for all three regions.

	MAM			**JJA**		
Region	30 to 35	35 to 40	40 to 45	30 to 35	35 to 40	40 to 45
All values	P-value ~ 0.0	P-value ~ 0.0	P-value ~ 0.0	P-value ~ 0.0	P-value ~ 0.0	P-value ~ 0.0
<40 dBZ	P-value ~ 0.0	P-value ~ 0.0	P-value ~ 0.0	P-value ~ 0.0	P-value ~ 0.0	P-value ~ 0.0
>40 dBZ	P-value = 0.681	P-value = 0.304	P-value = 0.442	P-value = 0.684	P-value = 0.672	P-value = 0.542

Table 4.1: Results of the Reflectivity Wilcoxon rank sum test between WRF CTRL and observed radar data.

	MAM			**JJA**		
Region	30 to 35	35 to 40	40 to 45	30 to 35	35 to 40	40 to 45
All values	P-value ~ 0.0	P-value ~ 0.0	P-value ~ 0.0	P-value ~ 0.0	P-value ~ 0.0	P-value ~ 0.0
<10 $mmhr^{-1}$	P-value ~ 0.0	P-value ~ 0.0	P-value ~ 0.0	P-value ~ 0.0	P-value ~ 0.0	P-value ~ 0.0
>10 $mmhr^{-1}$	P-value = 0.141	P-value = 0.224	P-value = 0.681	P-value = 0.231	P-value = 0.299	P-value = 0.689

Table 4.2: Results of the precipitation Wilcoxon rank sum test between WRF CTRL and observed Stage IV data.

Simulated reflectivity values above 40 dBZ were found to have similar distributions between WRF CTRL and WRF PGW with 95% confidence. The results of this testing are shown in Table 4.3 for all three sub-regions. Furthermore, the entire distribution of simulated reflectivity values and the stratiform (<40 dBZ) portion are also accepted to be similar, excluding R1 in MAM and R3 in JJA.

The simulated precipitation distribution as a whole and stratiform precipitation (>10 mm hr^{-1})

distribution comparison found, with 95% confidence, the WRF CTRL, and WRF PGW, were similar during MAM and JJA. This Wilcoxon testing is shown in Table 4.4. For simulated convective precipitation values (>10 mm hr^{-1}), during MAM, do not pass the test based on the confidence interval. Furthermore, during JJA R1 does not pass, but R2 and R3 do pass with P-values of 0.256 and 0.737, respectively.

	MAM			**JJA**		
Region	30 to 35	35 to 40	40 to 45	30 to 35	35 to 40	40 to 45
All values	P-value = 0.559	P-value = 0.598	P-value = 0.029	P-value = 0.771	P-value = 0.149	P-value = 0.328
<40 dBZ	P-value = 0.962	P-value = 0.705	P-value = 0.049	P-value = 0.037	P-value = 0.681	P-value = 0.795
>40 dBZ	P-value = 0.431	P-value = 0.251	P-value = 0.236	P-value = 0.338	P-value = 0.469	P-value = 0.969

Table 4.3: Results of the reflectivity Wilcoxon rank sum test between WRF CTRL and WRF PGW.

	MAM			**JJA**		
Region	30 to 35	35 to 40	40 to 45	30 to 35	35 to 40	40 to 45
All values	P-value = 0.236	P-value = 0.188	P-value = 0.401	P-value = 0.589	P-value = 0.562	P-value = 0.943
<10 $mmhr^{-1}$	P-value = 0.891	P-value = 0.277	P-value = 0.879	P-value = 0.191	P-value = 0.566	P-value = 0.266
>10 $mmhr^{-1}$	P-value = 0.005	P-value ~ 0.0	P-value ~ 0.0	P-value = 0.026	P-value = 0.256	P-value = 0.737

Table 4.4: Results of the precipitation Wilcoxon rank sum test between WRF CTRL and WRF PGW.

Both WRF CTRL and PGW have a higher simulated reflectivity interquartile range (IQR) than compared to the observations in all three sub regions, which suggests a higher variance of the model data values. The WRF CTRL and PGW reflectivity values have a lower maximum value in R1, but the observed maximum reflectivity values are lower in R2 and nearly the same as the

simulation in R1. These results are sown in Figure appendix 1 a, c, e box plots.

The observed IQR is less than the modeled IQR, and most of the model data points are all in the lower half of the distribution, as shown in the figure appendix (b, d, and f). This is an indication of WRF CTRL and PGW overestimating light precipitation since the simulated quantile 2 is well below the observed quantile 2. During JJA, the observed and historical simulated reflectivity show similar extreme distributions in R1, but in R1 and R2 the observed extreme distributions have more substantial outliers. In R2 and R3, the JJA observed maximum reflectivity values are much higher than modeled.

Moreover, the precipitation box plots (Figure Appendix 1 b, d, f) show the mean and IQR more central in the distribution. In these plots during MAM, the WRF CTRL simulated reflectivity IQR is larger, suggesting a higher variance in the data distribution. During JJA, the variance of the observed reflectivity is lower than the simulated reflectivity variance, but the observed reflectivity mean is higher. In MAM and JJA, the PGW 75^{th} percentile and maximum values slightly increase in all regions, but most in R3 during JJA. The precipitation box plots also show the observed precipitation data has higher extreme precipitation rates than compared to WRF CTRL for both seasons and all regions except for R2 in JJA and R1 in MAM. The WRF PGW spread of extreme values increases above the CTRL simulation for both seasons and all three regions.

A significant difference in the observed data compared to the simulation is the position of the quantile two (Q2) to quantile three (Q3) data range. The observed precipitation box plots are higher in both seasons and all three regions compared to the CTRL and PGW simulations. This result shows that the simulated precipitation data points are mostly made up of lower intensity rainfall rates. Comparing the data spread between the historical simulation and PGW climate projection, the PGW simulation has a higher maximum value than compared to the CTRL run.

4.2 Population Distribution

Though the WRF simulation overestimates extreme light precipitation (Figure appendix B, D, F), for moderate precipitation intensities between the reflectivity ranges 15–40 dBZ, WRF CTRL underestimates the frequency of values compared to the observations. This result is shown in Figure 4.1 a, c where the model underestimates the frequency of these values by roughly 5% for each bin during MAM and JJA. WRF CTRL also underestimates convective reflectivity values (>40 dBZ) for both MAM and JJA. Though less significant (note the log scale), Figure 4.1 b, d shows the

simulated heavy extreme precipitation (>60 dBZ) frequencies being overestimated by WRF CTRL during MAM and JJA. Contrary to light and moderate precipitation, the simulation overestimates heavy extreme precipitation.

WRF CTRL simulates a similar precipitation distribution type during MAM and JJA but produces precipitation rates less frequently than the observations. This result is shown in Figure 4.2 a, c. During MAM, all precipitation rate frequencies are simulated less frequently than the observations, but during JJA the simulated heavy precipitation rates are become similar in frequency. Though less significant at these higher precipitation rates, Figure 4.2 b, d shows for the histogram bins near 60 mm hr^{-1} and above, the observations and WRF CTRL are more similar in frequency. The MAM extreme high observed precipitation rates (Figure 4.2 b) also show the CTRL and PGW simulations underestimate these precipitation rates (> 100 $mmhr^{-1}$) similar to Figure 4.1 b where reflectivity values above 50 dBZ are also underestimated by both simulations.

The simulated reflectivity histogram comparison (Figure 4.1 a, c) show a similar distribution of values between WRF CTR and WRF PGW simulations. However, during MAM and JJA (Figure 4.1 b, d), WRF CTRL has a higher percentage of light reflectivity values, while the heavy precipitation (>40 dBZ) are simulated more frequently in WRF PGW for both seasons, though these heavy reflectivity values are far less frequent. The WRF PGW histogram shows similar frequency of precipitation rates compared to the CTRL distribution for light to moderate precipitation frequencies, as shown in Figure 4.2. However, the WRF PGW distribution gradually increases more in frequency compared to the WRF CTRL model as the precipitation rate increases.

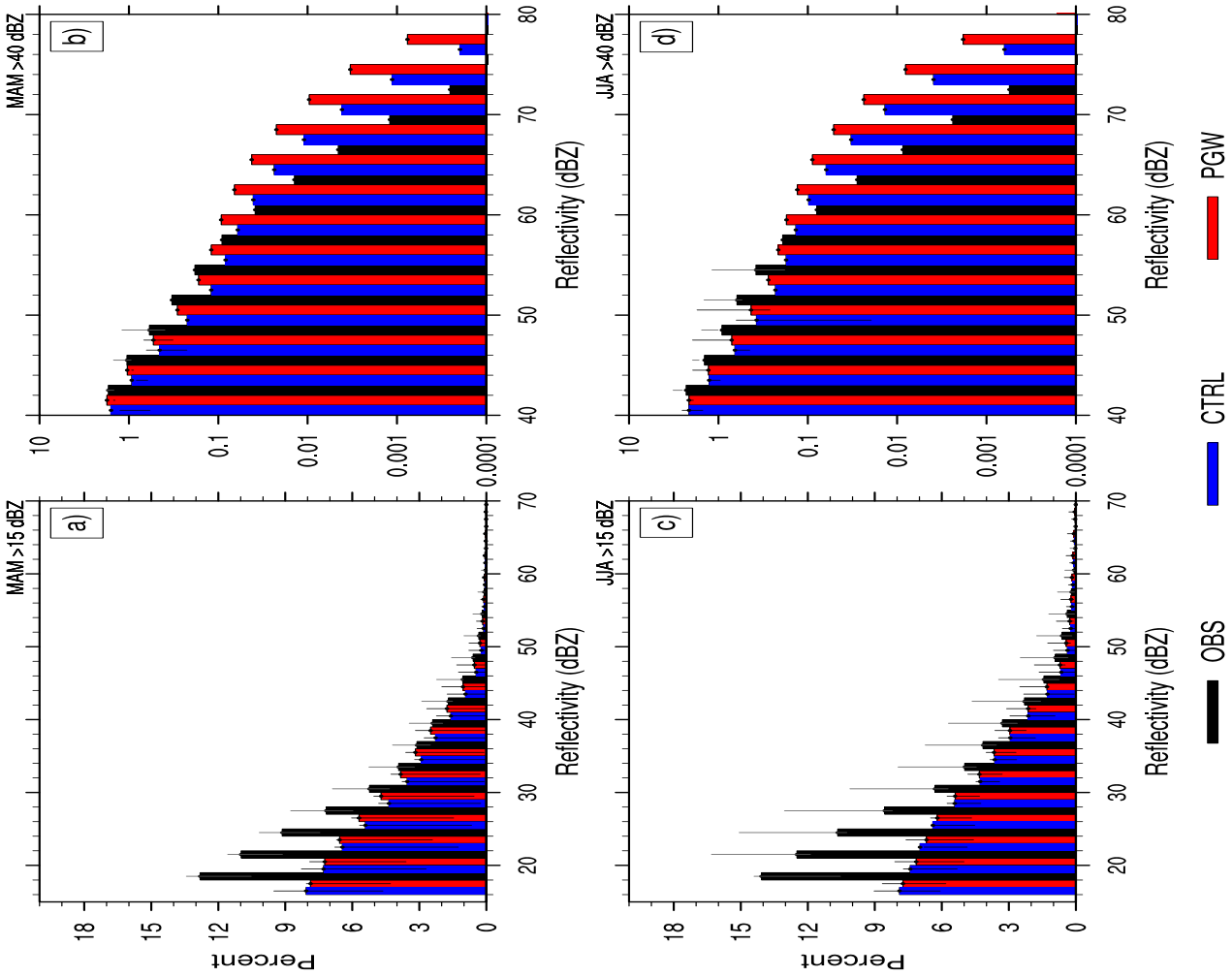

Figure 4.1: Histograms of simulated reflectivity from WRF CTRL, WRF PGW, and observed reflectivity during MAM (top) and JJA (bottom) for values greater than 15 dBZ (left) and values greater than 40 dBZ (right). The bars show the inter-annual variability (7 years for observations, WRF-CTRL, and WRF-PGW).

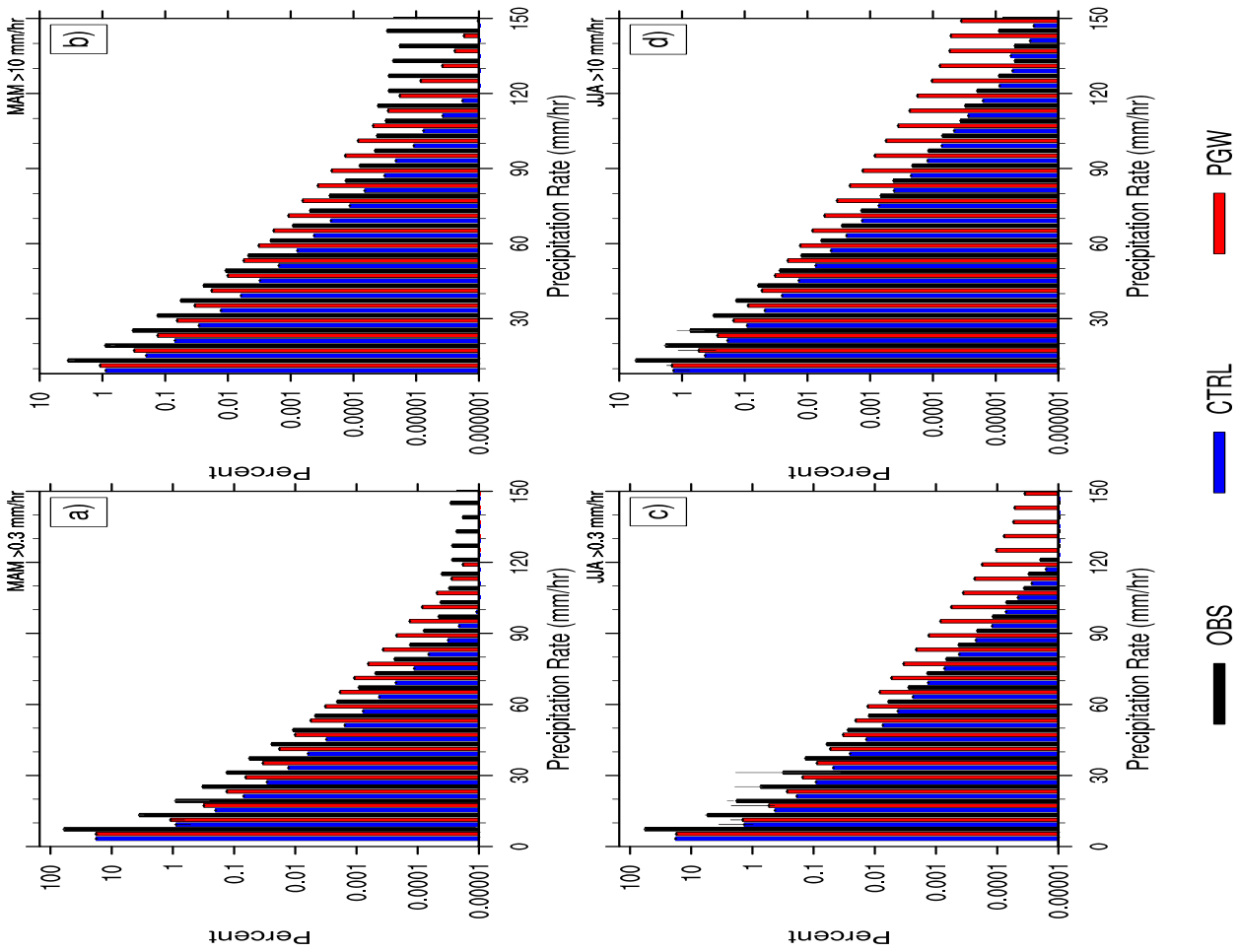

Figure 4.2: Histograms of simulated precipitation from WRF CTRL, WRF PGW, and observed precipitation during MAM (top) and JJA (bottom) for rain rates above 0.3 mmhr^{-1} (left) and rain rates above 10 mmhr^{-1} (right). The bars show the inter-annual variability (7 years for observations, WRF-CTRL, and WRF-PGW).

4.3 Diurnal Cycle Analysis

WRF CTRL overestimates reflectivity frequency values between the times of 16–02 UTC, or 11–21 LST. This result is shown in Figure 4.3 a, c, which is for all reflectivity values. For values >40 dBZ (Figure 4.3 b, d), WRF CTRL overestimates the frequency of reflectivity values around 20–04 UTC, or 15–23 LST.

Contrary to the modeled diurnal cycle overestimating the observations during the afternoon and evening, the diurnal signal in MAM and JJA, the model underestimates reflectivity frequencies

from 08–14 UTC, or 03–09 LST (overnight and early morning). The diurnal precipitation cycle analysis reveals similar results between the Stage IV observed precipitation and WRF CTL simulated precipitation shown in Figure 4.4.

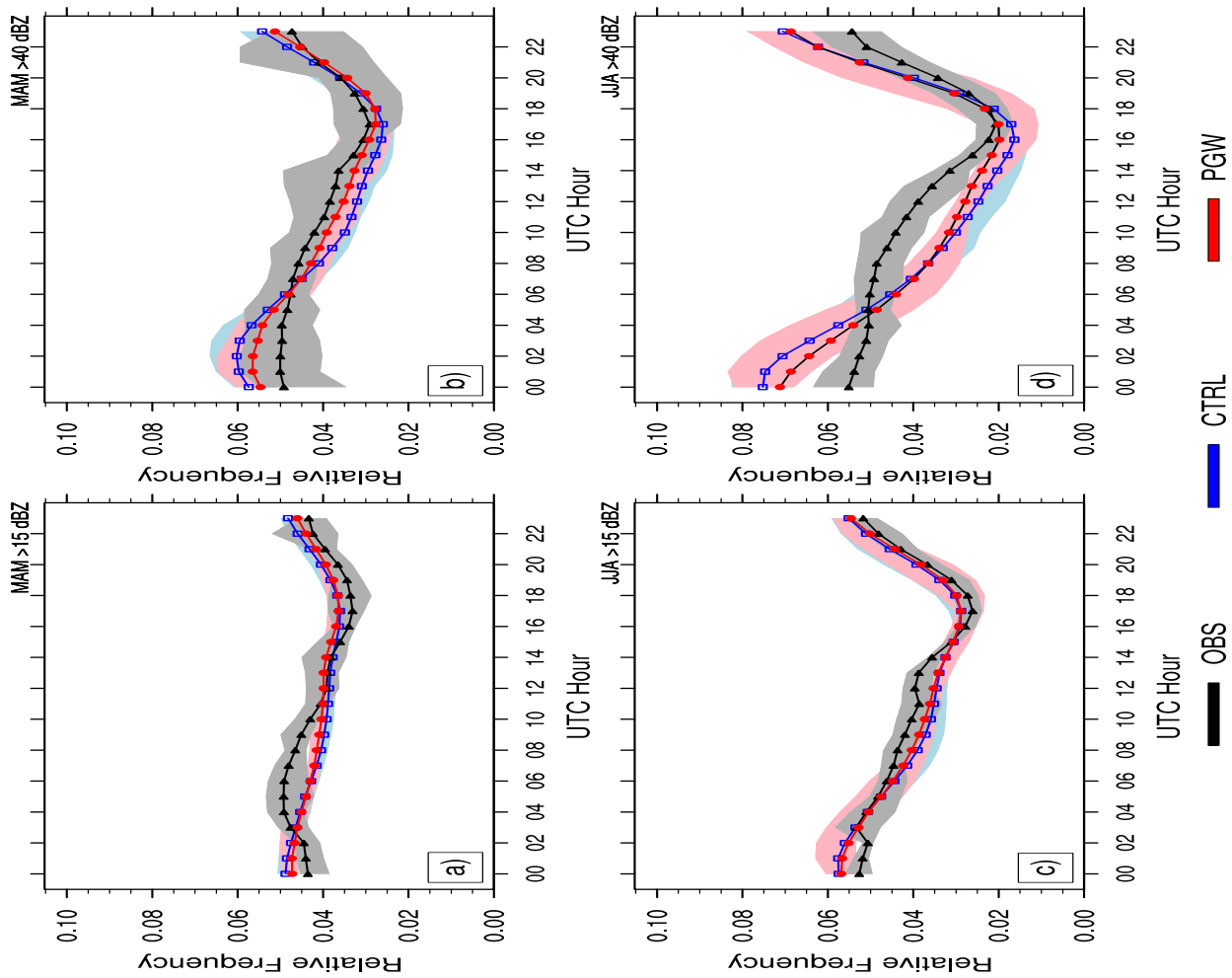

Figure 4.3: Diurnal cycle diagrams of simulated reflectivity from WRF CTRL, WRF PGW, and observed radar reflectivity during MAM (top) and JJA (bottom) for values above 0 dBZ (left) and values above 40 dBZ (right). The shaded area shows the inter-annual variability (7 years for observations, WRF-CTRL, and WRF-PGW).

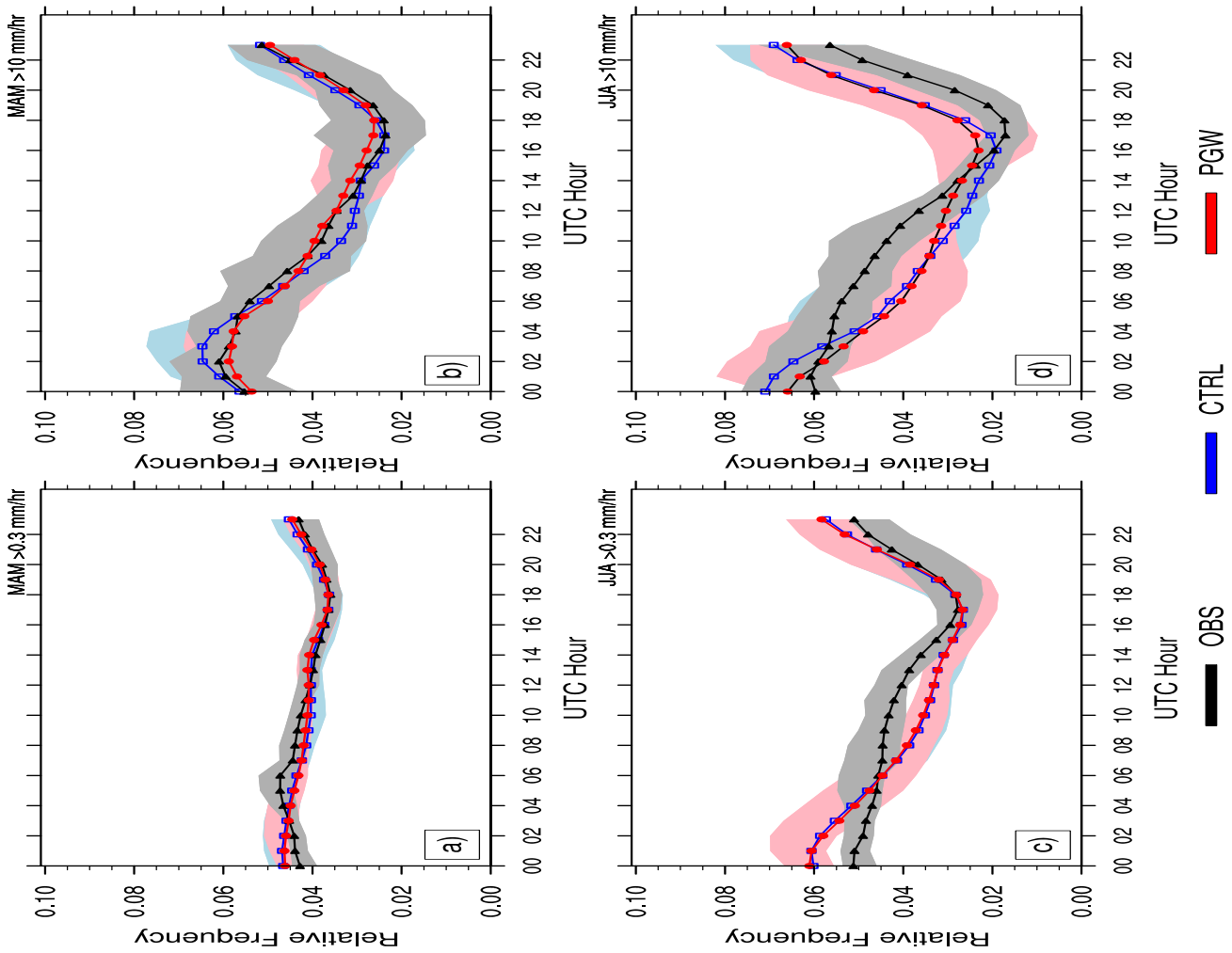

Figure 4.4: Diurnal cycle diagrams of simulated precipitation from WRF CTRL, WRF PGW, and observed Stage IV precipitation rate during MAM (top) and JJA (bottom) for values greater than 0.3 $mmhr^{-1}$ (left) and rain rates above 10 $mmhr^{-1}$ (right). The shaded area shows the inter-annual variability (7 years for observations, WRF-CTRL, and WRF-PGW).

Similar reflectivity frequencies occur over time between the CTRL model and PGW (Figure 4.3 a, c) model regarding all values, except from 07 to 15 UTC where the simulation underestimates precipitation frequency in JJA. The largest differences between the two simulations appear overnight where WRF PGW produces reflectivity and precipitation frequencies more similar to the observed diurnal pattern between 10 to 14 UTC. This result is shown in Figures 4.3 and 4.4 b (MAM), but is less significant in 4.4 d (JJA).

4.4 Hovmöller Diagrams

The hovmöller plots show significant feature differences between the model and observed reflectivity frequencies (Figures 4.5–4.12). During MAM for reflectivity (Figure 4.5), when the warm season diurnal cycle begins to intensify, the model does not match the observations as well in the lower latitude band, with a CC values (top right corner Figures j–o) around 0.6 to 0.8 with R3 being the closer comparison between the observations and WRF CTRL frequencies. 105 ºW initialization of observed precipitation around 20 to 02 UTC is present, then propagation eastward through the overnight hours.

The WRF CTRL reflectivity frequencies decrease overnight, while in the observations another local maximum in frequency can be seen around 90 ºW to 95 ºW at 12 UTC (07 LST), as shown in Figure 4.5 and 4.7. In R1, there is a closer comparison between the observations and model, but for the two higher latitude bands, the model has more deficiencies in simulating nocturnal precipitation. In R1 and R2, during MAM, the observations do not show high reflectivity frequency near 105 ºW, but rather just farther east near 103 ºW. However, low reflectivity frequencies are equivalent farthest west during the early morning through the afternoon. Farther east, around 95 ºW, during overnight hours there is a local maximum in reflectivity frequency in the observations and is well captured by the model.

WRF CTRL is able to simulate the propagation of storms eastward over time, but is insufficient in simulating nocturnal propagation. This result is shown in Figure 4.6 j, l, n. WRF CTRL compared to the observations results in areas of maximum reflectivity frequency for the central plains and lower Mississippi river valley from 04−12 UTC (11−07 LST) where WRF CTRL storm system propagation ends (negative difference values). The CTRL–OBS figures show the CTRL model overestimates the relative frequency of precipitation in this area, by over 90% in some areas, especially just leeward of the Rockies (Figure 4.9, 4.10 j, l, n), then an underestimation as time increases. There is also a considerable overestimation in reflectivity frequencies for WRF CTRL compared to the observations during MAM. This can be seen in Figure 4.9 j, l, n where areas of reflectivity above 40 dBZ which the WRF CTRL overestimates the observed convective frequencies during MAM, specifically for R1 (Figure 4.9 n).

The reflectivity hovmöller diagrams comparing WRF CTRL to WRF PGW simulations show similar patterns in areas of minimum and maximum frequency that show storm propagation for all three regions during MAM. During both seasons in R1, the frequency of reflectivity values both

decrease overnight, but the PGW simulation shows a more abrupt cutoff, while the CTRL model shows frequencies extending past 12 UTC (sunrise). This result is also evident in JJA for R2, but less so for MAM. Inside R1, the difference between the observations and CTRL (Figures 4.6 and 4.8 j, l, n) show higher differences during MAM, but less difference in relative frequency for JJA. However, during JJA the area just leeward of the Rockies does show a more significant difference in relative frequency by around 60 percent. An increase in reflectivity frequencies above 40 dBZ for PGW in the R2 region (Figure 4.9 m) also occurs. The hovmöller diagrams in Figure 4.11 k, m, o show a substantial increase in MAM for WRF PGW simulated convective precipitation, and similarly for R3 in JJA (Figure 4.12 k).

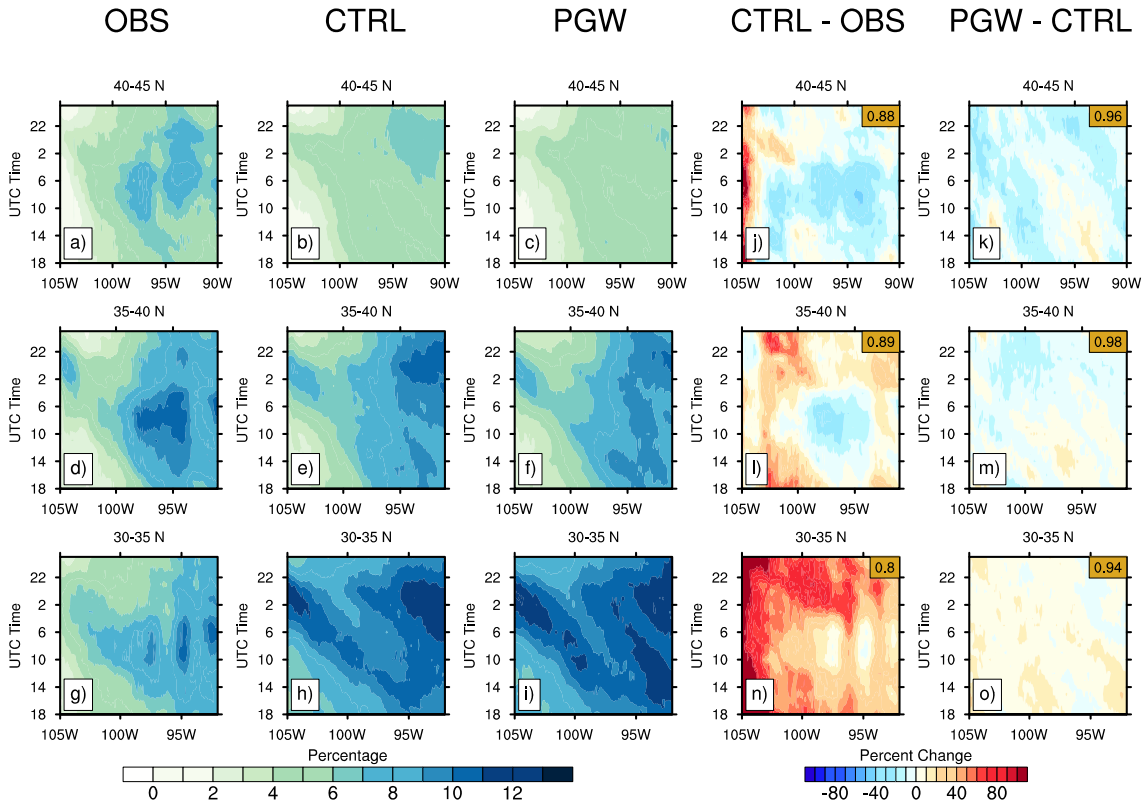

Figure 4.5: Observed radar reflectivity and WRF CTRL and WRF PGW simulated reflectivity hovmöller diagrams and percent change diagrams for CTRL–OBS and PGW–CTRL during MAM for values above 15 dBZ.

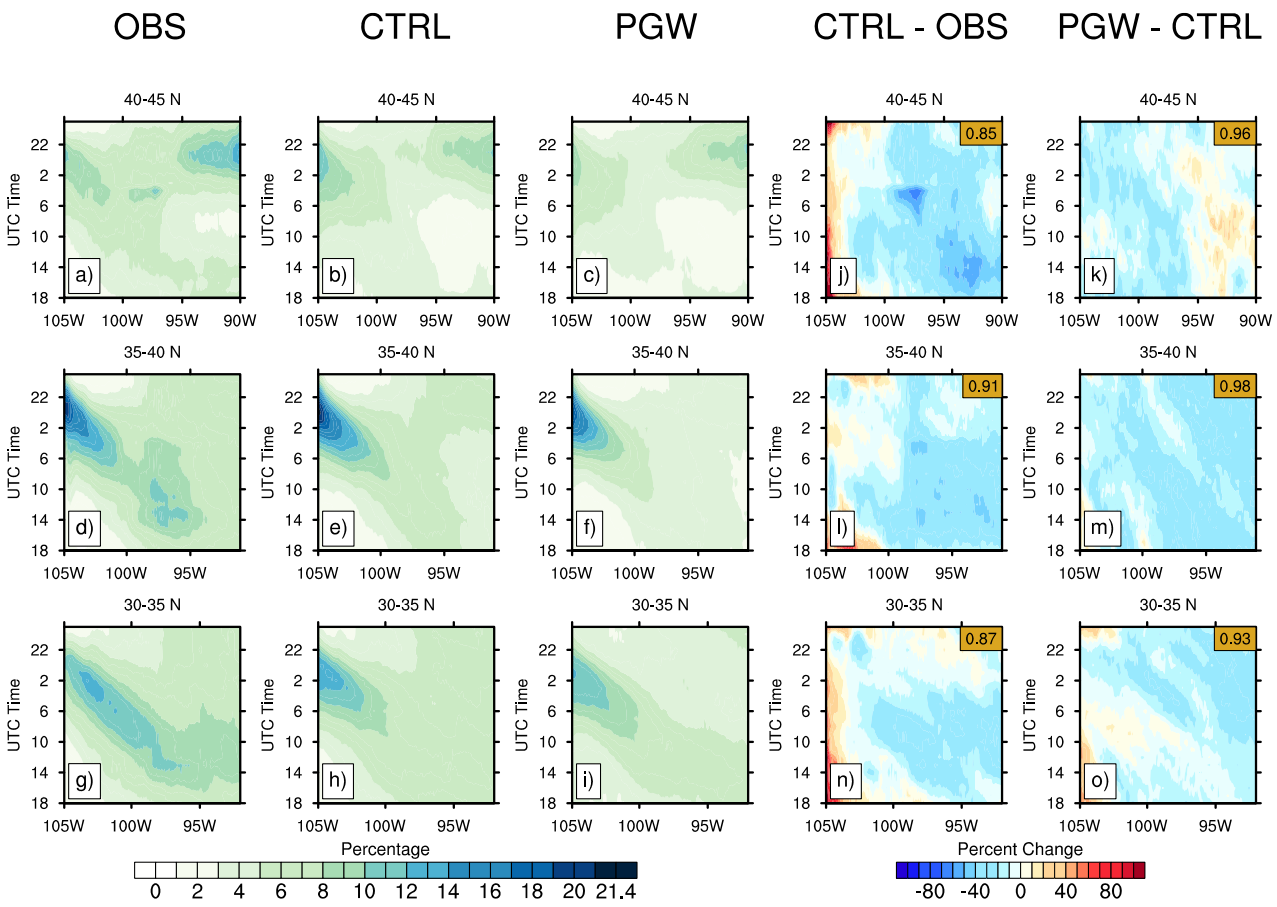

Figure 4.6: Observed radar reflectivity and WRF CTRL and WRF PGW simulated reflectivity hovmöller diagrams and percent change diagrams for CTRL–OBS and PGW–CTRL during JJA for values above 15 dBZ.

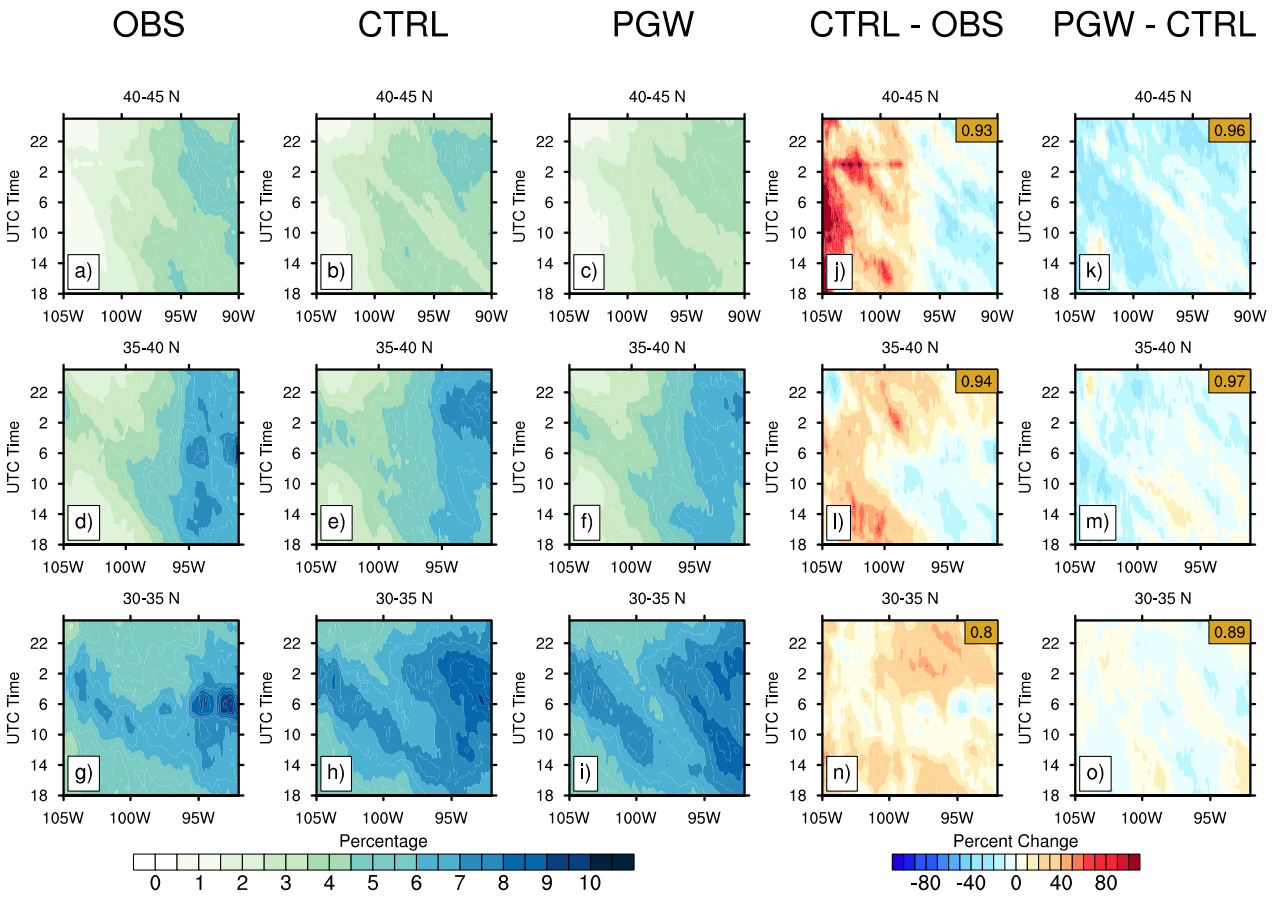

Figure 4.7: Observed Stage IV precipitation rate and WRF CTRL and WRF PGW simulated precipitation rate hovmöller diagrams and percent change diagrams for CTRL–OBS and PGW–CTRL during MAM for values above 0.3 $mmhr^{-1}$.

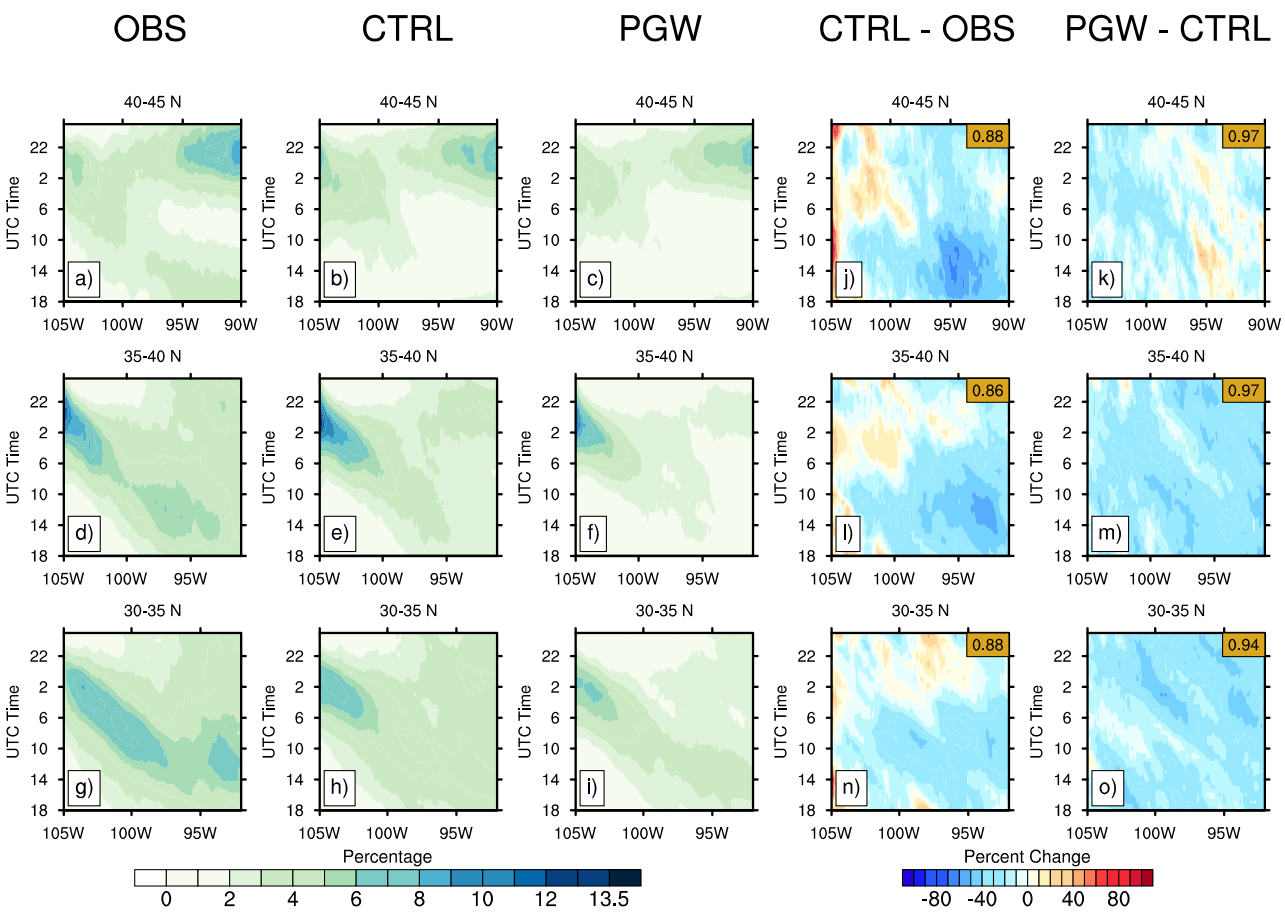

Figure 4.8: Observed Stage IV precipitation rate and WRF CTRL and WRF PGW simulated rain rate hovmöller diagrams and percent change diagrams for CTRL–OBS and PGW–CTRL during JJA for values above 0.3 $mmhr^{-1}$.

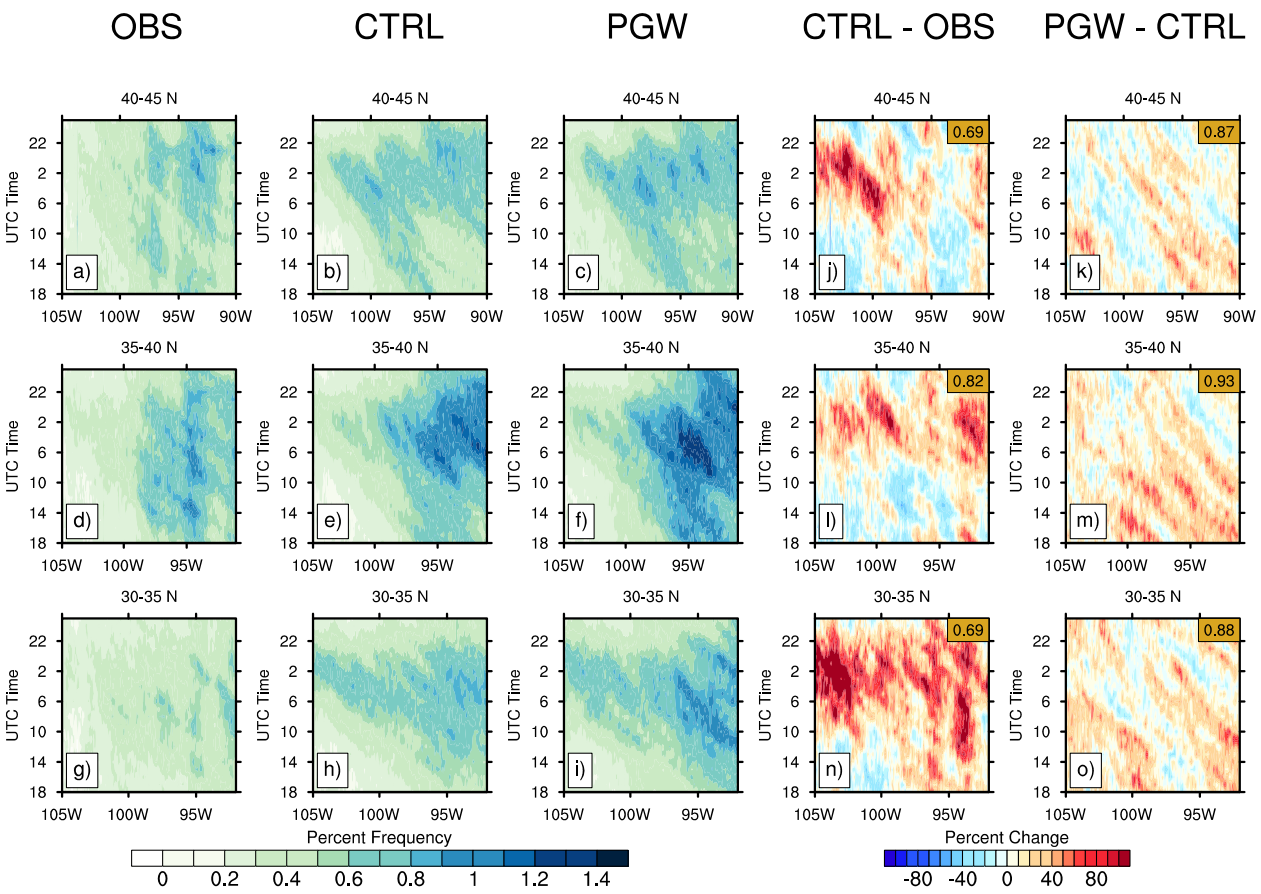

Figure 4.9: Observed reflectivity and WRF CTRL and WRF PGW simulated reflectivity hovmöller diagrams and percent change diagrams for CTRL–OBS and PGW–CTRL during MAM for values above 40 dBZ.

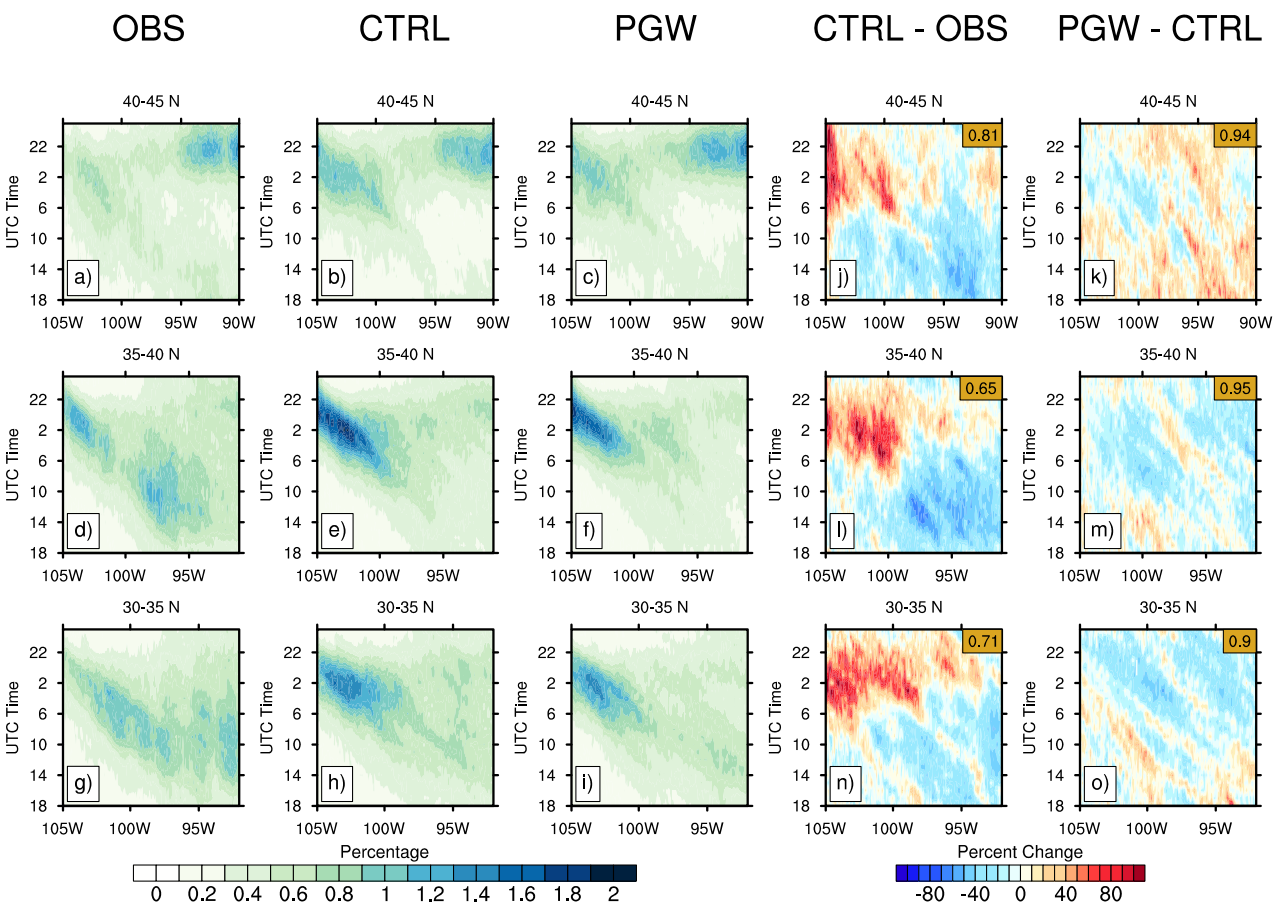

Figure 4.10: Observed reflectivity and WRF CTRL and WRF PGW simulated reflectivity hovmöller diagrams and percent change diagrams for CTRL–OBS and PGW–CTRL during JJA for values above 40 dBZ.

The convective (>40 dBZ) reflectivity hovmöller diagrams, in general, show similar patterns of propagation for both seasons and all three latitude bands. However, for convection in WRF PGW shows a slight increase in frequency for R2 and R3. In these areas, the frequency of reflectivity values above 40 dBZ decrease by 40%, with CC values ~0.7 and 0.8. Conversely, the R1 region shows a slight decrease in >40 dBZ reflectivity frequencies from the historical model to future projection. In MAM, the propagation in the PGW simulation decreases in frequency near 100 ºW at 04 UTC, while the historical model shows propagation continuing past 100 ºW until about 08 UTC (early morning). The convective precipitation (>10 mm hr^{-1}) hovmöller diagrams in MAM and JJA (Figures 4.11 and 4.12) also show similar patterns of propagation for both seasons and all three latitude bands. However, similar to the reflectivity hovmöller diagrams showing >40 dBZ, the PGW simulation shows an increase in convective precipitation frequency, especially for R1 and R2.

Additionally, convective initiation (CI) near 105 ºW varies significantly from historical to future projection in MAM. In R1, the convective initiation longitude is similar, but in the future projection, the frequency of this CI decreases by around 30%. However, in R2, CI near 105 ºW increases slightly in WRF PGW, but convection more significantly increased farther East during MAM. A similar difference occurs in R3 where the convection frequency increases farther East, but also mostly throughout the convective propagation in that area. Furthermore, in JJA for R3, the convection frequency increases more, by around 25%. In JJA for both R1 and R2, similar propagation patterns are present, and the change in convection frequency varies, with the CC value in these regions being 0.69 and 0.55 respectively.

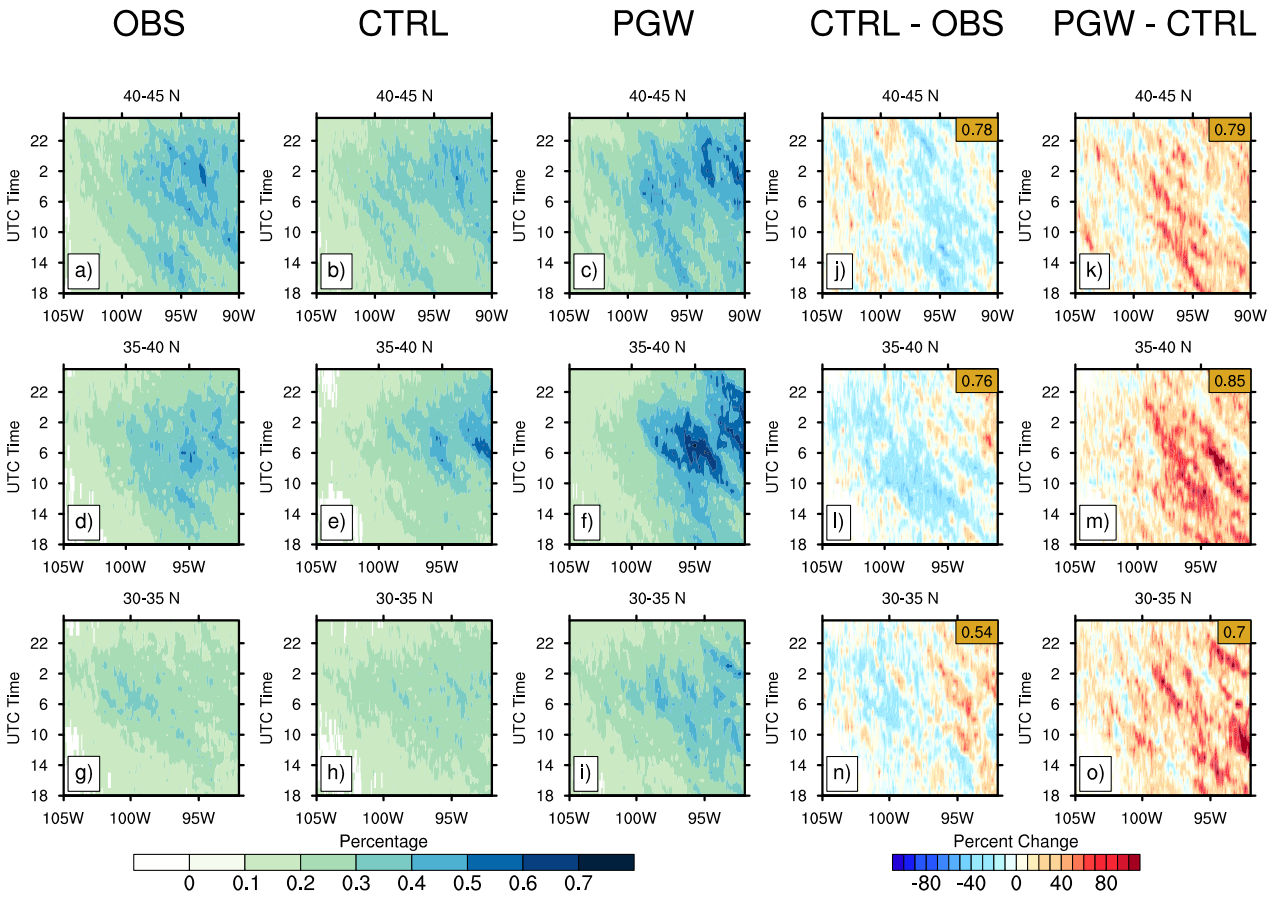

Figure 4.11: Observed Stage IV precipitation rate and WRF CTRL and WRF PGW simulated convective rainfall rate hovmöller diagrams and percent change diagrams for CTRL–OBS and PGW–CTRL during MAM for values above 10 mmhr^{-1}.

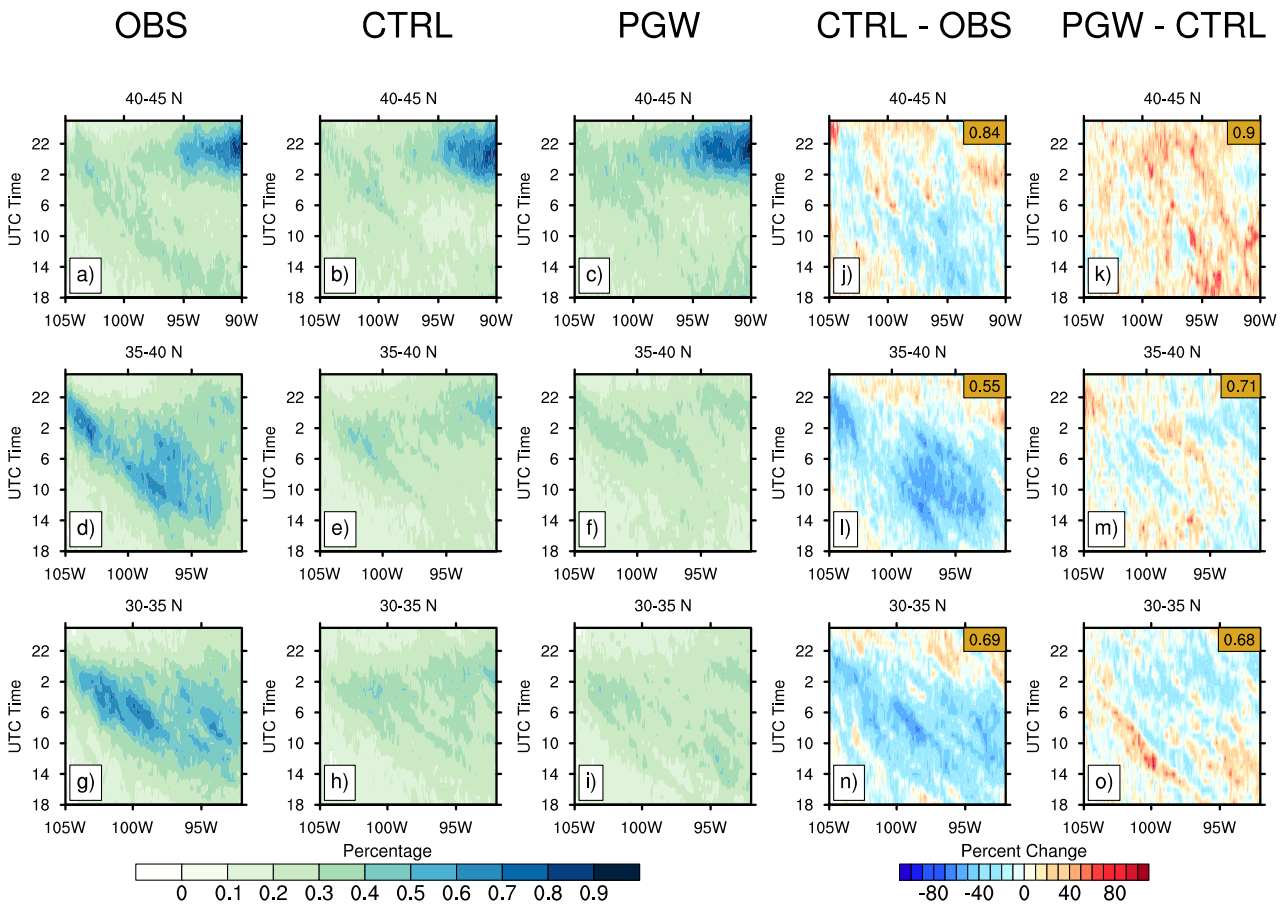

Figure 4.12: Observed Stage IV convective rain rate and WRF CTRL and WRF PGW simulated convective rain rate hovmöller diagrams and percent change diagrams for CTRL–OBS and PGW–CTRL during JJA for values above 10 mmhr^{-1}.

4.5 WRF CTRL and PGW Extreme Reflectivity and Precipitation Comparison

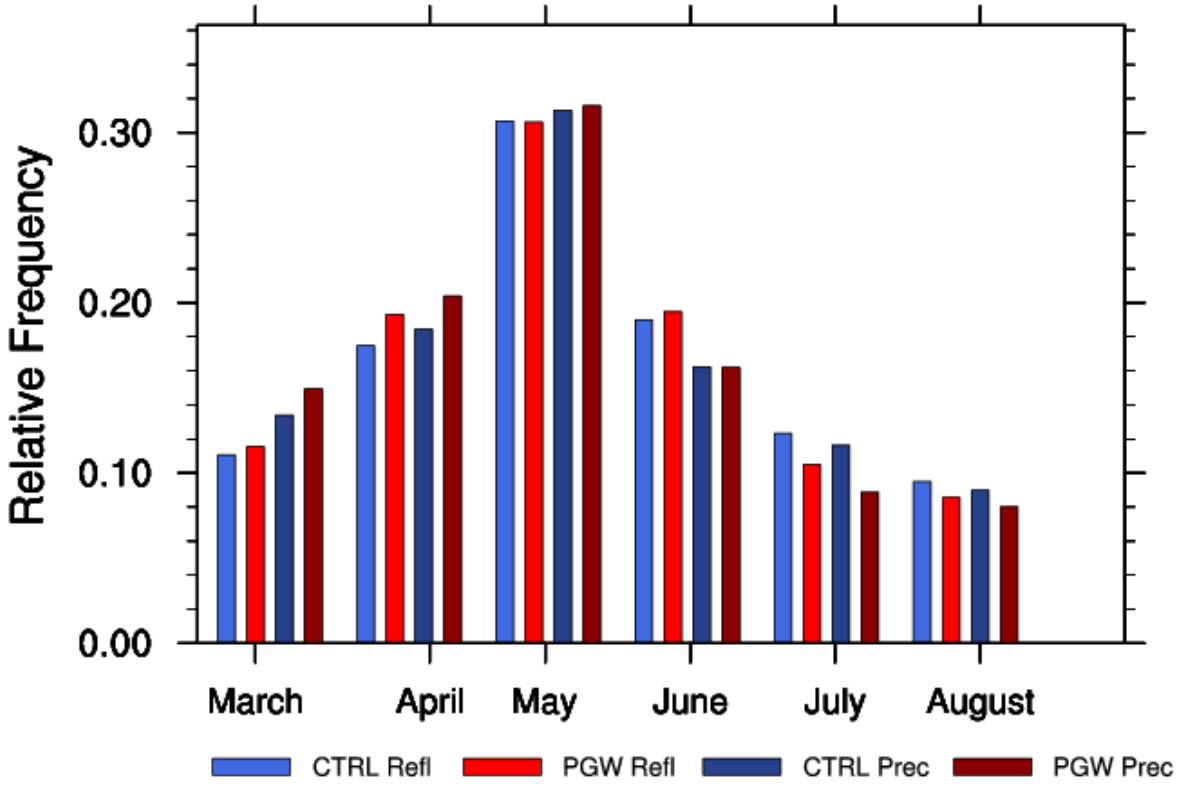

Figure 4.13: WRF CTRL and WRF PGW simulated reflectivity and precipitation monthly relative frequency for extreme (upper 99th percentile) values.

Frequency of extreme precipitation relative to the monthly occurrence of values exceeding the 99th percentile of seasonal reflectivity and precipitation data is shown in Figure 4.13. This figure compares the change between the historical climate to the PGW projected climate. The occurrence of extreme values from the upper 99th percentile is found for each month, then the frequency relative to all warm season months for each variable is found. While a predicted increase in future precipitation is present in MAM, there is a projected decrease for the PGW projection during JJA.

Although JJA mostly shows a decrease in extreme precipitation occurrence, this may be related to the warm/dry bias present in the simulation. The increase in precipitation frequency is possibly due to the increase of the environmental temperature, the amount of water vapor that can be held by a saturated parcel of air will also increase (Hartmann 2015). This is more evident early in the spring season, with a less significant increase in May and June.

Chapter 5. Discussion

5.1 Statistical Discussion

Most of the precipitation data are made up of values less than 5 mm hr^{-1} with the mode between 0.3 and 5 mm hr^{-1}. Thus, most of the stratiform precipitation data is made up of minimal values, i.e., stratiform precipitation less than 10 mm hr^{-1} (mist and very light rain). Therefore, large differences in frequency of stratiform precipitation causes significant differences in the statistical test results between stratiform and convective reflectivity values, which are less frequent but more similar. Also, For all precipitation rate values; the WRF CTRL simulation is consistently underestimating precipitation rates compared to Stage IV for MAM and through 70 mm hr^{-1} during JJA, causing the test to not pass.

In the model statistical testing, the WRF CTRL and PGW simulations compared the distributions showed that for both MAM and JJA, the convective reflectivity distributions pass the statistical test with 95% confidence that the two distributions are similar. Only the R3 in MAM for all values and stratiform distribution fail the test in MAM, and R1 stratiform distribution in JJA fails the simulated reflectivity Wilcoxon rank-sum test. In the simulated precipitation statistical testing, all of the distribution and stratiform data values accept the null hypothesis that the distributions are similar. However, the convective distributions fail in all three regions during MAM and only R1 in JJA, suggesting that, with 95% confidence, that the WRF CTRL and PGW convective distributions differ. Supported by the histograms, this result shows where the PGW convective precipitation distribution begins to deviate more from the CTRL with more extreme precipitation rates (Figure 4.2 b, d).

5.2 Population Distribution

The WRF simulation produces too much light to moderate precipitation, as shown in the box plots. This overestimation in the model may arise from errors in the microphysics scheme that produce too much light rain and mist in the model. A study done to improve bulk microphysics schemes suggests autoconversion (collision coalescence of cloud droplets) as a significant problem in parameterizing microphysical processes in models (Stoelinga et al. 2003). The authors suggest that

errors in model microphysics schemes such as cloud concentration number, cloud droplet concentration, or entrainment effects mainly impact autoconversion and is not well parameterized in simulations. As the microphysics scheme produces a non-zero reflectivity value at any level, this shows up in the composite column maximum simulated reflectivity variable. Thus, many light reflectivity values found in the model occur where no observed radar reflectivity values are present.

In MAM, the precipitation distribution (Figure 4.2 a, b) the simulation is deficient in producing high precipitation rates compared to the observations. This deficiency may be related to a lack of short duration convective precipitation events produced in the simulation. Short duration convective precipitation events are especially challenging to simulate correctly due to the smaller scale forcing mechanisms, and the spatially localized nature of the precipitation.

This light precipitation overestimation may also be related to the warm/dry bias (which may include some convective storms also) discussed in Liu et al. (2016). The authors believe the central U.S. summer bias in temperature and precipitation due to errors in the solar radiation, surface heat transport, and soil moisture in this area. These variables can have a significant effect in determining surface moisture flux and cloud-resolving convection. The underestimation of light to heavy precipitation in the model is also believed to occur from the model not initiating convection leeward of the Rockies and the High Plains region. This model deficiency was quantified in Prein et al. (2017). The authors showed that during JJA, the model underestimates MCS frequency (light to moderate precipitation) by 75% compared to the observations. Even though the horizontal resolution is 4-km, individual convective cells can only be generated at this scale, while in many cases in nature, is too large.

Though light to moderate reflectivity has the most considerable underestimation by the model, reflectivity values above 40 dBZ and precipitation rates above 10 mm hr^{-1} are underestimated by the model, also. In both MAM and JJA, the model underestimates convective precipitation rates. The observed precipitation rates range up to 60 mm hr^{-1} while the model only simulates a far smaller percentage of precipitation rates only up to 30 or 40 mm hr^{-1}. Similar to Gutowski et al. (2003), the modeled precipitation intensities are underestimated compared to the observation data.

Light and moderate precipitation does not change significantly in the PGW model, but convective and extreme precipitation is increasing more (Figure 4.2 b, d). Increase in precipitation extremes is likely to happen due to the net warming that has already occurred (IPCC AR4 2014), and the warming is expected to continue to happen while the world produces more greenhouse gases. While the histograms show light to moderate precipitation frequency increasing, the

precipitation bins become increasingly more frequent for more intense rainfall rates in WRF PGW compared to WRF CTRL.

5.3 Diurnal Cycle Analysis

Normalized frequency over time (UTC) bar charts were created to analyze the diurnal cycle of radar reflectivity and precipitation. The results of these plots show how the model can capture the phase of the diurnal cycle reasonably well but overestimates the amplitude. The error in the model concerning both seasons and hours of the day shows how the model overestimates the amplitude of the diurnal cycle.

This observed result agrees with Stelten and Gallus (2017), who performed a climatology study of the observed nocturnal convection initiation during the PECAN experiment. However, the model only shows one diurnal peak, and also matches with the first peak of the observations at 04 UTC, late evening local time. The observed bimodal diurnal peak may be related to zonal variations in the diurnal cycle across the analysis domain.

In both MAM and JJA, the CTRL simulation underestimates nocturnal convection frequency. As discussed earlier, although solar insolation plays a large part in producing late afternoon and evening convection, nocturnal convection persists due to propagating cold pools, undular bores (gravity waves), and potential vorticity production over the Rocky Mountains and High Plains region. This underestimation of nocturnal MCS's may be related to mesoscale processes not simulated well due to gravity wave and cold pool propagation occurring on scales smaller than the model horizontal resolution (Engerer et al. 2008).

The convective reflectivity (>40 dBZ) diurnal peak is higher in JJA than compared to MAM, and during both seasons, the modeled diurnal cycle has a higher amplitude of frequency (relative frequencies of 0.060, 0.080) than the observed diurnal cycle (relative frequencies of 0.050, 0.055) (MAM, JJA respectively). The model exaggerating the diurnal amplitude is thought to be from overestimating convective initiation and underestimating nocturnal MCS propagation as thunderstorms move eastward. Similar results occur between the Stage IV observed precipitation and WRF CTL simulated precipitation (Figure 4.4). This lack of MCS propagation is also a result of the hovmöller diagrams in the next section.

For values >40 dBZ in MAM, the model overestimated the frequency of values between 20–04 UTC, but also underestimated values between 08–18 UTC, about late morning local time. This

error in the model occurs where the overestimated peak frequency occurs, and nocturnal convection is underestimated in the central U.S. This finding is in line with Prein et al. (2017) who studied MCS track density for the Eastern half of the U.S. leeward of the Rockies. This study showed that the model overestimates MCS frequency in the High Plains near 105° W, then underestimate MCS frequency in the central plains.

The WRF CTRL model has a deficiency with lack of convection overnight in the central plains, as shown earlier. If the model has trouble producing convection overnight compared to observations, this will be likely for the future projection also. Assuming this error occurs in the PGW simulation, there will be less modeled convection in the early evening, but more convection than shown in the overnight hours.

During MAM and JJA, the comparison between all reflectivity values is similar. However, the model was shown to be deficient in producing overnight convection in the central plains. This bias slightly occurs in MAM, but is more prevalent in JJA, as the warm season precipitation diurnal cycle is beginning in MAM, and full swing during JJA. However, a dry bias in JJA dominating the central U.S. has been studied in Liu et al. (2016) who conclude that a deficiency from feedback loops of solar radiation and clouds, soil moisture, and heat/moisture transport may be present. Errors in these model processes have a tremendous impact on accurately simulating the diurnal precipitation cycle.

According to Liu et al. (2016), the percent change of MAM precipitation between WRF CTRL and PGW simulations is roughly a 20 percent increase for the central U.S. From figure 4.4 c, d, in JJA, there is about a 20 percent decrease in precipitation for the central (R2) and north-central Great Plains (R3), but a 30% increase in precipitation for the southern plains (R1).

The CTRL model has deficiencies in simulating nocturnal convection, but in the future projection, the frequency of this precipitation is shown to increase. The model may have difficulties simulating these processes and feedback loops. Soil moisture may have the most notable impact on this warm and dry bias, however. This bias is a significant issue for numerical modeling considering a study done by Koster et al. (2004) found that the central USGP as a center for maximum for land/atmosphere coupling strength, therefore it is crucial for the model to simulate these processes accurately.

5.4 Hovmöller diagrams

Time as a function of longitude maps was used to analyze the central U.S. thunderstorm propagation from west to east over time. The split analysis domain is into 5 degree latitude bands ranging from 30 ºN–35 ºN (R1), 35 ºN to 40 ºN (R2), and 40 ºN to 45 ºN (R3) with the same longitudinal range as the analysis domain from 105 ºW to 90 ºW. In creating these diagrams, data were analyzed in the 5 degree latitude band for each set of UTC hours (00 to 23) to find the percent frequency of the reflectivity and precipitation values. Then the frequency of the values were averaged latitudinally for each sub region. As a result, time is plotted as a function of longitude to see the areas of the maximum frequency of reflectivity values propagate eastward over each UTC hour.

The location and timing of the observed and modeled convective initiation agreed with the study done by Carbone and Tuttle (2008) where the authors analyzed observed radar data in the central U.S. and found that rainfall was present 65% of the time at 105 ºW during 2100 UTC. The observed reflectivity frequencies propagate eastward overnight and into the late morning until around 95 ºW. However, in the model, the reflectivity frequencies begin to decrease around 08–12 UTC near 100 ºW. For R3, the frequency values show accurate comparisons from 105 ºW to 100 ºW, with a CC value of 0.78. Conversely, in the central plains and eastward, the model produces reflectivity values later in the afternoon and early evening while the observations show more reflectivity values overnight. Nocturnal precipitation has been a longtime deficiency in numerical models conducted for the central plains (Surcel et al. 2010, Trenberth et al. 2003) where an underestimation of overnight precipitation occurs in the simulation.

In R1, in MAM and JJA most of the propagation starts after 18 UTC in both the radar and precipitation plots. In R2, similar maximums in the frequency of both radar and precipitation occur here. Specifically, the frequency maximum near 95 ºW at 06 UTC is in both the radar and precipitation hovmöller diagrams. However, this area varies between the model and observations. In the radar plots during MAM, the model shows a maximum slightly earlier near or just before 02 UTC (including a higher maximum near 105 ºW instead of just between 95 ºW and 90 ºW). In JJA, for R2 there is closer comparison where the maximum frequency areas are both near 105 ºW and 95 ºW to 90 ºW, with a CC value of 0.86.

The observations show more frequent precipitation around 12 UTC close to 90 ºW. In the CTRL simulation, these frequencies are often underestimated, possibly due to the LLJ not being simulated correctly. According to Trier, Davis, and Ahijevych 2010, overnight propagation linked with the LLJ intensity and direction is a mechanism that contributes to the slower eastward

progression of maximum diurnal frequencies. This feature occurs in the observations where the propagation of precipitation frequencies slow down, i.e., more horizontal area of frequencies. In the CTRL simulation, these frequencies are often underestimated, or not shown at all.

Southern U.S. nocturnal underestimation of precipitation was studied previously and thought to be a contributing factor to the warm and dry bias in this model (Liu et al. 2017). This bias could be due to the 4-km grid being too coarse to simulate cold pool MCS propagation and undular bores which help initiate and propagate nocturnal thunderstorms (Haghi 2018). The results of this study clearly show model deficiencies in simulating nocturnal precipitation. A cause of this may be due to coarse horizontal grid spacing not being able to simulate cold pool propagation, but also undular bores which help initiate and propagate MCSs by aiding in air parcel lift which are not fully resolved in a 4-km resolution simulation (Johnson et al. 2017, Degelia et al. 2018). Also, the 4-km modeled grid has a downfall in simulating large scale convective movements which have been shown to result in large convective cells not entraining midlevel air (Bryan and Morrison 2012).

Throughout spring and summer leeward of the Rockies, a dry line forms where dry air to the west meets moist air from the east, the Gulf of Mexico being a primary source of moisture. Hence, in this area, the LLJ is vital in transferring moisture which aids in nocturnal precipitation (Higgins 1997). In this region (R1 and R2 mainly), possible areas of decreased precipitation frequency in figure 4.8 and 4.10 j, k, l, m, n, o, and in R1 during JJA, precipitation has some decrease in frequency but mostly increase in Figure 4.10. Although WRF CTRL also shows some decrease in precipitation frequency, this may be related to a model deficiency. However, the nocturnal precipitation maximum over the central U.S. may slowly shift northward during the spring and summer months from the Gulf Coast toward the upper Midwest. As a result of climate change, there may be a shift in agriculture production in this part of the country.

5.5 Climate Change Assessment Discussion

With processes that cause the greenhouse effect, the global average temperature of the Earth may increase over the next century. Due to this feedback mechanism, anthropogenic climate change will occur from an increase in greenhouse gases. Humans are continuing to produce more and more CO_2 (burning fossil fuels), CH4 (burning biofuels), and N2O (agriculture) (IPCC AR5 2014). Furthermore, the latest IPCC special report on land-climate interactions predicts with high confidence that the current warming of land surface air temperature is projected to result in new, warmer climates

in mid to high latitudes due to a shift in climate zones poleward (IPCC SRCCL 2019). This projection is according to the globally averaged land surface air temperature (LSAT) that shows a rising global mean surface temperature (the combined LSAT and sea surface temperature) from preindustrial (1850–1900) to present day (1999–2018).

From the PGW simulation, there is a predicted increase in future precipitation, and this increase becomes more extensive with high precipitation rates (Figure 4.18). The increase in extreme precipitation events could be due to the model simulating more extreme rainfall and even large hail (extreme reflectivity) more in the future projection (Emori and Brown 2005, Willett et al. 2007, and Kunkel et al. 2013). The water vapor feedback can cause this due to an increase of the environmental temperature, the amount of water vapor that can be held by a saturated parcel of air will also increase (Hartmann 2015, O'Gorman and Muller 2010). The PGW simulation uses RCP 8.5, so an increase in CO_2 would have a warming effect increasing the water vapor capacity of the air, in turn, creating more intense precipitating storms.

The hovmöller diagrams show an increase in reflectivity frequency above 40 dBZ and precipitation frequency during MAM in the PGW simulation (Figure 4.9 and 4.11 c, k, f, m, i, o), particularly for the two northern latitude bands that were analyzed. However, in the precipitation hovmöller diagrams in the lowest latitude band, the relative frequency of convection increases in the PGW projection compared to the CTRL simulation. In R2, the relative frequencies of convection remain relatively similar. In the northernmost latitude band, there is an increase of about 0.2% in MAM and 0.3% in JJA.

The WRF CTRL and PGW hovmöller comparison diagrams (PGW–CTRL Figures 4.5 to 4.12 m, n, o) show the percent change between the historical simulation and PGW simulation. Some areas of the hovmöller comparison are similar to WRF CTRL while others (both spatially and seasonally) differ widely. During MAM, all reflectivity and precipitation data (Figures 4.7 and 4.9) in the PGW hovmöller diagrams closely match the WRF CTRL hovmöller diagrams. This result is quantified in the spatial CC analysis, with values from 0.91 to 0.97, indicating a higher (better) correlation. This result is also evident for all data values in JJA with CC values from 0.94 to 0.99, also denoting better correlation.

However, during this time, and mainly for MAM, for convective precipitation (>10 mm hr^{-1}), the hovmöller comparison diagrams show areas of substantial-frequency increase. This increase in convective precipitation occurrence is mainly from 00 to 12 UTC around 95 ºW, most evident in R2, and less evident in R1. The CC values also supports this evidence. For MAM convective precipitation,

the PGW–CTRL CC value in R2 is lowest at 0.85, and highest in R3 at 0.79, with R3 being in the middle at 0.7.

An increase in air temperature, according to the Clausius Clapeyron relation, may also lead to an increase in extreme weather frequency. Studies have shown that the increase of global surface temperatures caused by anthropogenic climate change is expected to intensify the hydrologic cycle (Huntington 2006, O'Gorman and Schneider 2009, and Trenberth et al. 2003). With the water vapor feedback loop, this intensifies the greenhouse warming effect. Through an increase in temperature, the amount of water vapor in the saturated air parcel increases also.

This increase in precipitation leads to the hypothesis that a future increase of greenhouse gas emissions leads to a future intensification of thunderstorms in the central U.S. Since warmer air can lead to increase in moisture, the warm air can contain more water vapor. Due to the model simulating warmer average temperatures in the lower troposphere, leading to higher moisture content and therefore more yearly precipitation. The evidence for the increase in near-surface temperature is shown in Liu et al. (2016). A result of this study found that in the central U.S., there was an increase of 2-meter temperature by about 4 ºC in the annual mean temperature.

Thus, thunderstorms that form in a warmer environment can produce more rain (Hartmann 2015). However, a limitation to this assumption is that the WRF model was biased low in comparison to the Stage IV observed precipitation rate. Nonetheless, a positive feedback loop may still occur. Assuming relative humidity remains nearly constant (Hartmann 2015) while surface air temperature varies in a warmer climate, increasing the water vapor content amplifies the greenhouse effect, thus raising the temperature even further.

The impact from this feedback has been studied and shown to lead to more frequent extreme rainfall events and changes in the intensity and frequency of precipitation (Allen and Ingram 2002, Allan and Soden 2008, Dai 2013, Held and Soden 2006). Due to the abundance of moisture transport from the LLJ, including other factors that contribute to nocturnal development of MCSs (Bonner 1968, Arritt et al. 1997). It has been found that the majority of warm-season precipitation over the USGP is convective, with a significant percentage (>25%) occurring overnight (Higgins et al. 1997, Changnon 2001) and coinciding with the nocturnal LLJ (Bonner, 1968). Thus, leading to the hypothesis of a future increase in temperature in the central U.S. combined with moisture transport from the LLJ, which may lead to more frequent and severe convective precipitation in the USGP.

This increase in extreme precipitation may have an impact on the future U.S. agriculture production. As of 2017, the top ten agricultural producing U.S. states were, in decreasing order,

California, Iowa, Texas, Nebraska, Minnesota, Illinois, Kansas, North Carolina, Wisconsin, and Indiana (USDA 2018). Five of these ten states make up a large portion of the analysis domain for this study; thus, the future of the precipitation in this area of the country is of great importance. One estimate study using a WRF simulation showed results that the USGP would see an increase in precipitation frequency due to more moisture transport from the LLJ occurring early in the warm season (MAM) (Harding and Snyder 2014). While the change in spatial frequency of precipitation in the USGP remains uncertain and a possible increase in water resource demands in the future, this area of the country may be impacted dramatically by climate change.

Chapter 6. Summary and Conclusion

This study examined a WRF convection-permitting model's capabilities of simulating warm-season convection in the central United States. The simulated reflectivity distribution, the diurnal cycle of precipitation, and storm propagation were compared to observations. This study uses seven years of observed hourly precipitation and radar data to evaluate and assess the model simulation. Also studied was the increase in greenhouse gas emissions impact on precipitation in a future climate.

Overall, similar characteristics of propagating precipitation systems exist between the observations and the WRF simulation, including the initiation and propagation of convective systems. Seasonally, WRF overestimates the frequency of reflectivity values in MAM, while under-producing convective systems in JJA during the day. The model's most considerable difficulty lies in simulating nocturnal convection. Additionally, the WRF simulation frequently overproduces mist and extreme light precipitation (0–15 dBZ). During MAM and JJA, moderate reflectivity values, between 20–40 dBZ, are underestimated by the WRF simulation while comparing to observed reflectivity. In MAM, the WRF model underestimates reflectivity values around 08–14 UTC (nocturnal convection). Similarly, during JJA, WRF CTRL simulated diurnal cycle peaks at 23–06 UTC, significantly exceeding the amplitude of the OBS. Propagation of storms eastward occurs on the hovmöller diagrams, but while the peak of observed late afternoon precipitation is similar, the WRF model underestimates the frequency values and propagation overnight.

The simulation warm and dry bias and deficiency in simulating nocturnal precipitation is partly due to the coarse horizontal grid spacing. Even though the 4-km horizontal resolution allows for explicit deep convection initialization, some fundamental mechanisms that help initiate and drive precipitation across the US are smaller than 4-km, such as simulating cold pool propagation and undular bores that play a role in nocturnal initiation of convection. Therefore, the model has trouble simulating these processes. Similarly, the coarse grid spacing also impacts the land surface model and as a result, the surface moisture flux representation in the model.

The climate projection key findings depict possible extreme weather event frequency increases; thus, the sustainability field should be aware of this possible outcome. This PGW simulation shows an increase in convection frequency for parts of the analysis domain. A significant climate change signal is an increase in extreme precipitation frequency, especially during summer. Results from this test show extreme precipitation frequencies in the PGW simulation increasing,

especially for MAM. This study of a WRF simulation and other climate simulations using the RCP greenhouse gas emissions scenarios have shown that if our society continues with "business as usual," there will be changes to the current climate over the next 80 years.

However, as the PGW simulation shows some increase in convective precipitation for many parts of the central US, it is precautionary to realize this may be linked to the historical model having deficiencies in accurately simulating the frequency of this precipitation. Though, the increase of extreme precipitation may have a substantial effect on the central US prairie water supply mainly used for agriculture and infrastructure. With other studies of WRF models showing similar results with increases in extreme precipitation frequency, the impact of anthropogenic caused climate change is a realistic possibility.

This WRF model, and therefore the results of this study, are primarily dependent on the emission scenarios used. These scenarios may change with human activities, particularly population growth, rate of economic development, and social policy implementation. Consequently, any change in the future emission levels will impact the projected climate changes in different ways, and thus impacts the future projections studied. Future climate projections are not consistent in climate models and emission scenarios. Similarly, a limitation to consider is the study period. This study refers 2071–2100 as the future period, thus the projected future impacts should be assumed as impacts for that period. Any change in the future will also change the results making the climate projections dissimilar to those in the study period. Also, consider that climate change projections and their confidence vary across different climate models (Teutschbein and Seibert, 2012).

The results of this study show that this convective permitting high-resolution NWP model can be valuable in simulating central US precipitation characteristics. In addition, possible impacts of climate change on future precipitation showed the warm and dry biases due to lack of small-scale forcing mechanisms (which can be explained by NWP model weaknesses). The simulation can be improved by adding the small-scale features to schemes that can trigger convection (in high spatial- and temporal resolutions).

Future research should further this study by using more than one climate model/emission scenario to provide a range of possible climate change impact estimates. Similarly, future research should focus on the model's quality outside the analysis region, such as the west and east parts of the US, southern Canada, and northern Mexico. More future studies could go more into depth on the direct impact of climate change on agriculture and society.

References

Ahrens, C. D. 2011: *Essentials of Meteorology: An Invitation to the Atmosphere*. Cengage Learning, 454 pp.

Allan, R. P., and B. J. Soden, 2008: Atmospheric warming and the amplification of precipitation extremes. *Science*, **321**, 1481–1484, https://doi.org/10.1126/science.1160787.

Allen, M. R., and W. J. Ingram, 2002: Constraints on future changes in climate and the hydrologic cycle. *Nature*, **419**, 228–232, https://doi.org/10.1038/nature01092.

American Meteorological Society, 2012: Glossary of Meteorology. Accessed 12 March 2019, http://glossary.ametsoc.org/wiki/Rain.

Arritt, R. W., T. D. Rink, M. Segal, D. P. Todey, C. A. Clark, M. J. Mitchell, and K. M. Labas, 1997: The Great Plains low-level jet during the warm season of 1993. *Mon. Wea. Rev.*, **125**, 2176–2192, https://doi.org/10.1175/1520-0493(1997)125<2176:TGPLLJ>2.0.CO;2.

Augustine, J. A., and F. Caracena, 1994: Lower-tropospheric precursors to nocturnal MCS development over the central United States. *Wea. Forecasting*, **9**, 116–135, https://doi.org/10.1175/1520-0434(1994)009<0116:LTPTNM>2.0.CO;2.

Ban N., J. Schmidli, C. Schär, 2014: Evaluation of the convection-resolving regional climate modeling approach in decade-long simulations. *J. Geophys. Res.*, **119**, 7889–7909, https://doi:10.1002/2014JD021478.

Bechtold, P., J. P. Chaboureau, A. Beljaars, A. K. Betts, M. Köhler, M. Miller, and J. L. Redelsperger, 2004: The simulation of the diurnal cycle of convective precipitation over land in a global model. *Quart. J. Roy. Meteor. Soc.*, **130**, 3119–3137, https://doi.org/10.1256/qj.03.103.

Bluestein, H. B. 2006: *Tornado alley: Monster Storms of the Great Plains*. Oxford University Press, 183 pp.

Bryan, G. H., H. Morrison, 2012: Sensitivity of a simulated squall line to horizontal resolution and parameterization of microphysics. *Mon. Wea. Rev*. **140**, 202–225, https://doi.org/10.1175/MWR-D-11-00046.1.

Bodine, D. J., K. L. Rasmussen, 2017: Evolution of mesoscale convective system organizational structure and convective line propagation. *Mon. Wea. Rev*., **145**, 3419–3440, https://doi.org/10.1175/MWR-D-16-0406.1.

Bonner, W. D., 1968: Climatology of the low level jet. *Mon. Wea. Rev.*, **96**, 833–850, https://doi.org/10.1175/1520-0493(1968)096<0833:COTLLJ>2.0.CO;2.

Brisson, E., K. Van Weverberg, M. Demuzere, A. Devis, S. Saeed, M. Stengel, and N. P. M. van Lipzig, 2016: How well can a convection-permitting climate model reproduce decadal statistics of precipitation, temperature and cloud characteristics? *Climate Dyn.*, **47**, 3043–3061, https://doi.org/10.1007/s00382-016-3012-z.

Bukovsky, M. S., R. R. McCrary, A. Seth, and L. O. Mearns, 2017: A mechanistically credible, poleward shift in warm-season precipitation projected for the US Southern Great Plains? *J. Climate*, **30**, 8275–8298, https://doi.org/10.1175/JCLI-D-16-0316.1.

Carbone, R. E., J. D. Tuttle, 2008: Rainfall occurrence in the US warm season: The diurnal cycle. *J. Climate*, **21**, 4132–4146, https://doi.org/10.1175/2008JCLI2275.1.

Changnon, S. A., 2001: Thunderstorm rainfall in the conterminous United States. *Bull. Amer. Meteor. Soc.*, **82**, 1925–1940, https://doi.org/10.1175/1520-0477(2001)082<1925:TRITCU>2.3.CO;2.

Chou, C., C. A. Chen, P. H. Tan, and K. T. Chen, 2012: Mechanisms for global warming impacts on precipitation frequency and intensity. *J. Climate*, **25**, 3291–3306, https://doi.org/10.1175/JCLI-D-11-00239.1.

Cooperative Distributed Interactive Atmospheric Catalog System/Earth Observing Laboratory/National Center for Atmospheric Research/University Corporation for Atmospheric Research, and Climate Prediction Center/National Centers for Environmental Prediction/National Weather Service/NOAA/U.S. Department of Commerce. 2000, updated quarterly. NCEP/CPC Four Kilometer Precipitation Set, Gauge and Radar. Research Data Archive at the National Center for Atmospheric Research, Computational and Information Systems Laboratory, accessed 08 August 2018, https://doi.org/10.5065/D69Z93M3.

Corfidi, S. F., 2003: Cold pools and MCS propagation: Forecasting the motion of downwind-developing MCSs. *Wea. Forecasting*, **18**, 997–1017, https://doi.org/10.1175/1520-0434(2003)018<0997:CPAMPF>2.0.CO;2.

Dai, A., F. Giorgi, K. E. Trenberth, 1999: Observed and model-simulated diurnal cycles of precipitation over the contiguous United States. *J. Geophys. Res.*, **104**, 6377–6402, https://doi.org/10.1029/98JD02720.

Dai, A., 2001: Global precipitation and thunderstorm frequencies. Part II: Diurnal variations. *J. Climate*, **14**, 1112–1128, https://doi.org/10.1175/1520-

0442(2001)014<1112:GPATFP>2.0.CO;2.

Dai, A., 2013: Increasing drought under global warming in observations and models. *Nature Climate Change*, **3**, 52–58, https://doi.org/10.1038/nclimate1633.

Degelia, S. K., X. Wang, D. J. Stensrud, and A. Johnson, 2018: Understanding the impact of radar and in situ observations on the prediction of a nocturnal convection initiation event on 25 June 2013 using an ensemble-based multiscale data assimilation system. *Mon. Wea. Rev.*, **146**, 1837–1859, https://doi.org/10.1175/MWR-D-17-0128.1.

Dee, D. P., and Coauthors, 2011: The ERA-Interim reanalysis: Configuration and performance of the data assimilation system. *Quart. J. Roy. Meteor. Soc.*, **137**, 553–597, https://doi.org/10.1002/qj.828.

Emori, S., and S. J. Brown, 2005: Dynamic and thermodynamic changes in mean and extreme precipitation under changed climate, *Geophys. Res. Lett.*, **32**, L17706, https://doi.org/10.1029/2005GL023272.

Engerer, N. A., D. J. Stensrud, and M. C. Coniglio, 2008: Surface characteristics of observed cold pools. *Mon. Wea. Rev.*, **136**, 4839–4849, https://doi.org/10.1175/2008MWR2528.1.

Fabry, F., 2012: Daily and annual cycles of precipitation and convection over the continental United States. *Proc. Seventh European Conf. on Radar in Meteorology and Hydrology*, Toulouse, France, Météo-France, 5 pp., http://www.meteo.fr/cic/meetings/2012/ERAD/extended_abs/RCS_089_ext_abs.pdf.

Feng, Z., L. R. Leung, S. Hagos, R. A. Houze, C. D. Burleyson, K. Balaguru, 2016: More frequent intense and long-lived storms dominate the springtime trend in central US rainfall. *Nature Comms.* **7**, https://doi.org/10.1038/ncomms13429.

Fosser, G., S. Khodayar , P. Berg, 2014: Benefit of convection permitting climate model simulations in the representation of convective precipitation. *Climate Dyn.*, **44**, 45–60, https://doi.org/10.1007/s00382-014-2242-1.

Frei, C., C. Schär, D. Lüthi, and H. C. Davies, 1998: Heavy precipitation processes in a warmer climate. *Geophys. Res. Lett.*, **25**, 1431–1434, https://doi.org/10.1029/98GL51099.

Fritsch, J. M., J. R. Kane, C. R. Chelius, 1986: The contribution of mesoscale convective weather systems to the warm-season precipitation in the United States. *J. Climate Appl. Meteor.*, **25**, 1333–1345, https://doi.org/10.1175/1520-0450(1986)025<1333:TCOMCW>2.0.CO;2.

Fournier, J. D., 1999: Reflectivity-rainfall rate relationships in operational meteorology. National Weather Service Technical Memo, 6 pp, https://www.weather.gov/tae/research-zrpaper.

Geerts, B., and Coauthors, 2017: The 2015 plains elevated convection at night field project. *Bull. Amer. Meteor. Soc.*, **98**, 767–786, https://doi.org/10.1175/BAMS-D-15-00257.1.

Giorgi, F., G. T. Bates, 1989: On the climatological skill of a regional model over complex terrain. *Mon. Wea. Rev.*, **117**, 2325–2347, https://doi.org/10.1175/1520-0493(1989)117<2325:TCSOAR>2.0.CO;2.

Gray, W. M., and R. W. Jacobson Jr, 1977: Diurnal variation of deep cumulus convection. *Mon. Wea. Rev.*, **105**, 1171–1188, https://doi.org/10.1175/1520-0493(1977)105<1171:DVODCC>2.0.CO;2.

Gutowski, W. J., S. G. Decker, R. A. Donavon, Z. Pan, R. W. Arritt, and E. S. Takle, 2003: Temporal–spatial scales of observed and simulated precipitation in central US climate. *J. Climate*, **16**, 3841–3847, https://doi.org/10.1175/1520-0442(2003)016<3841:TSOOAS>2.0.CO;2.

Guttman, N. B., and C. B. Baker, 1996: Exploratory analysis of the difference between of the difference between temperature observations recorded by ASOS and conventional methods. *Bull. Amer. Meteor. Soc.*, **77**, 2865–2873, https://doi.org/10.1175/1520-0477(1996)077<2865:EAOTDB>2.0.CO;2.

Haghi, K. R., and Coauthors, 2019: Bore-ing into Nocturnal Convection. *Bull. Amer. Meteor. Soc.*, **100**, 1103–1121, https://doi.org/10.1175/BAMS-D-17-0250.1.

Hamilton, K., 1981: A note on the observed diurnal and semidiurnal rainfall variations. *J. Geophys. Res.*, **86**, 12122–12126, https://doi.org/10.1029/JC086iC12p12122.

Hartmann, D. L. 2015: *Global Physical Climatology*. Newnes, 473 pp.

Held, I. M., and B. J. Soden, 2006: Robust responses of the hydrological cycle to global warming. *J. Climate*, **19**, 5686–5699, https://doi.org/10.1175/JCLI3990.1.

Higgins, R. W., Y. Yao, E. S. Yarosh, J. E. Janowiak, and K. C. Mo, 1997: Influence of the Great Plains low-level jet on summertime precipitation and moisture transport over the central United States. *J. Climate*, **10**, 481–507, https://doi.org/10.1175/1520-0442(1997)010<0481:IOTGPL>2.0.CO;2.

Houze, R. A., 1973: A climatological study of vertical transports by cumulus-scale convection, *J. Atmos. Sci.*, **30**, 1112–1123, https://doi.org/10.1175/1520-0469(1973)030<1112:ACSOVT>2.0.CO;2.

Huntington, T. G., 2006: Evidence for intensification of the global water cycle: review and synthesis. *J. Hydrol.*, **319**, 83–95, https://doi.org/10.1016/j.jhydrol.2005.07.003.

Iacono, M. J., J. S. Delamere, E. J. Mlawer, M. W. Shephard, S. A. Clough, and W. D. Collins, 2008: Radiative forcing by long-lived greenhouse gases: Calculations with the AER radiative transfer models. *J. Geophys. Res.*, **113**, D13103, https://doi.org/10.1029/2008JD009944.

IPCC, 2014: Climate Change 2014: Synthesis Report. Contribution of Working Groups I, II and III to the Fifth Assessment Report of the Intergovernmental Panel on Climate Change [Core Writing Team, R.K. Pachauri and L.A. Meyer (eds.)]. IPCC, Geneva, Switzerland, 151.

IPCC, 2019: Climate Change and Land: an IPCC special report on climate change, desertification, land degradation, sustainable land management, food security, and greenhouse gas fluxes in terrestrial ecosystems. [Core Writing Team, G. Jia and E. Shevliakova (eds.)]. SRCCL, Geneva, Switzerland, 186.

Johnson, A., X. Wang, S. K. Degelia, 2017: Design and implementation of a GSI-based convection-allowing ensemble data assimilation and forecast system for the PECAN field experiment. Part II: Overview and evaluation of a real-time system. *Wea. Forecasting*, **32**, 1227–1251, https://doi.org/10.1175/WAF-D-16-0201.1.

Kain, J. S., S. J. Weiss, D. R. Bright, M. E. Baldwin, J. J. Levit, 2006: Examination of convection-allowing configurations of the WRF model for the prediction of sever convective weather: The SPC/NSSL Spring program 2004. *Wea. Forecasting*, **21**, 167–181, https://doi.org/10.1175/WAF906.1.

Karl, T. R., and K. E. Trenberth, 2003: Modern global climate change. *Science*, **302**, 1719–1723, https://doi.org/10.1126/science.1090228.

Kawase, H., T. Yoshikane, M. Hara, F. Kimura, T. Yasunari, B. Ailikun, and T. Inoue, 2009: Intermodel variability of future changes in the Baiu rainband estimated by the pseudo global warming downscaling method. *J. Geophys. Res.*. **114**, https://doi.org/10.1029/2009JD011803.

Kendon, E., and Coauthors, 2016: Do convection-permitting regional climate models improve projections of future precipitation change? *Bull. Amer. Meteor. Soc.*, **98**, 79–93, https://doi.org/10.1175/BAMS-D-15-0004.1.

Koster, R. D., and Coauthors, 2004: Regions of strong coupling between soil moisture and precipitation. *Science*, **305**, 1138–1140, https://doi.org/10.1126/science.1100217.

Kraus, E. B., 1963: The diurnal precipitation change over the sea. *J. Atmos. Sci.*, **20**, 551–556, https://doi.org/10.1175/1520-0469(1963)020<0551:TDPCOT>2.0.CO;2.

Kunkel, K. E., D. R. Easterling, D. A. Kristovich, B. Gleason, L. Stoecker, and R. Smith, 2010: Recent increases in US heavy precipitation associated with tropical cyclones. *Geophys. Res.*

Lett., **37**, L24706, https://doi.org/10.1029/2010GL045164.

Kunkel, K. E., and Coauthors, 2013: Monitoring and understanding trends in extreme storms: State of knowledge, *Bull. Amer. Meteor. Soc.*, **94**, 499–514, https://doi.org/10.1175/BAMS-D-11-00262.1.

LaDue, D. S., P. L. Heinselman, and J. F. Newman, 2010: Strengths and limitations of current radar systems for two stakeholder groups in the southern plains. *Bull. Amer. Meteor. Soc.*, **91**, 899–910, https://doi.org/10.1175/2009BAMS2830.1.

Lang, S., W. K. Tao, J. Simpson, and B. Ferrier, 2003: Modeling of convective–stratiform precipitation processes: Sensitivity to partitioning methods. *J. Appl. Meteor.*, **42**, 505–527, https://doi.org/10.1175/1520-0450(2003)042<0505:MOCSPP>2.0.CO;2.

Liang, X. Z., L. Li, A. Dai, K. Kunkel, 2004: Regional climate model simulation of summer precipitation diurnal cycle over the united states. *Geophys. Res. Lett.*, **31**, L24208, https://doi.org/10.1029/2004GL021054.

Lima, M.A., and J. W. Wilson, 2008: Convective storm initiation in a moist tropical environment. *Mon. Wea. Rev.*, 13**6**, 1847–1864, https://doi.org/10.1175/2007MWR2279.1.

Liu, C., and Coauthors, 2016: Continental-scale convection-permitting modeling of the current and future climate of North America. *Climate Dyn.*, **49**, 71–95, https://doi.org/10.1007/s00382-016-3327-9.

Liu, J., C. Folberth, H. Yang, J. Röckström, K. Abbaspour, and A. J. Zehnder, 2013: A global and spatially explicit assessment of climate change impacts on crop production and consumptive water use. *PLoS ONE*, **8**, e57750, https://doi.org/10.1371/journal.pone.0057750.

Lott, N., and T. Ross, 2006: Tracking and Evaluating US Billion Dollar Weather Disasters, 1980-2005. NOAA National Climatic Data Center, Accessed 12 March 2019, https://www.ncdc.noaa.gov/monitoring-content/billions/docs/lott-and-ross-2006.pdf.

McGuire, V.L., 2017: Water-level and recoverable water in storage changes, High Plains aquifer, predevelopment to 2015 and 2013–15: U.S. Geological Survey Scientific Investigations Report 2017–5040, 16 pp, https://doi.org/10.3133/sir20175040.

Mearns, L. O., and Coauthors, 2012: The North American Regional Climate Change Assessment Program: Overview of Phase I Results. *Bull. Amer. Meteor. Soc.*, **93**, 1337–1362, https://doi.org/10.1175/BAMS-D-11-00223.1.

Moore, N., and S. Rojstaczer, 2002: Irrigation's influence on precipitation: Texas High Plains, USA. *Geophys. Res. Lett.*, **29**, 2–1, https://doi.org/10.1029/2002GL014940.

Moore, J. T., F. H. Glass, C. E. Graves, S. M. Rochette, and M. J. Singer, 2003: The environment of warm-season elevated thunderstorms associated with heavy rainfall over the central United States. *Wea. Forecasting*, **18**, 861–878, https://doi.org/10.1175/1520-0434(2003)018<0861:TEOWET>2.0.CO;2.

Nelson, B. R., D. J. Seo, D. Kim, 2010: Multisensor Precipitation Reanalysis. *J. Hydrometeor*., **11**, 666–682, https://doi.org/10.1175/2010JHM1210.1.

Niu, G. Y., and Coauthors, 2011: The community Noah land surface model with multiparameterization options Noah-MP): 1. Model description and evaluation with local-scale measurements. *J. Geophys. Res.*, **116**, D12109, https://doi.org/10.1029/2010JD015139.

O'Gorman, P. A., and C. J. Muller, 2010: How closely do changes in surface and column water vapor follow Clausius–Clapeyron scaling in climate change simulations? *Env. Res. Lett.*, **5**, 025207, http://dx.doi.org/10.1088/1748-9326/5/2/025207.

Pall, P., M. R. Allen, and D. A. Stone, 2007: Testing the Clausius–Clapeyron constraint on changes in extreme precipitation under CO_2 warming. *Climate Dyn*., **28**, 351–363, https://doi.org/10.1007/s00382-006-0180-2.

Parish, T. R., and L. D. Oolman, 2010: On the role of sloping terrain in the forcing of the Great Plains low-level jet. *J. Atmos. Sci*., **67**, 2690–2699, https://doi.org/10.1175/2010JAS3368.1.

Penide, G., A. Protat, V. V. Kumar, and P. T. May, 2013: Comparison of two convective/stratiform precipitation classification techniques: Radar reflectivity texture versus drop size distribution–based approach. *J. Atmos. Oceanic Technol.*, **30**, 2788–2797, https://doi.org/10.1175/JTECH-D-13-00019.1.

Prein, A. F., G. J. Holland, R. M. Rasmussen, J. Done, K. Ikeda, M. P. Clark, and C. H. Liu, 2013: Importance of regional climate model grid spacing for the simulation of heavy precipitation in the Colorado headwaters. *J. Climate*, **26**, 4848–4857, https://doi.org/10.1175/JCLI-D-12-00727.1.

Prein, A. F., and Coauthors, 2015: A review on regional convection-permitting climate modeling: Demonstrations, prospects, and challenges. *Rev. of Geophys.*, **53**, 323–361, https://doi.org/10.1002/2014RG000475.

Prein, A. F., C. Liu, K. Ikeda, R. Bullock, R. M. Rasmussen, G. J. Holland, M. Clark, 2017: Simulating North American Mesoscale Convective Systems with a convection-permitting climate model. *Climate Dyn.*, 1–16, https://doi.org/10.1007/s00382-017-3993-2.

Prein, A. F., R. M. Rasmussen, K. Ikeda, C. Liu, M. P. Clark, G. J. Holland, 2016: The future

intensification of hourly precipitation extremes. *Nature Climate Change*, **7**, 48–52, https://doi.org/10.1038/nclimate3168.

Ramanathan, V., P. J. Crutzen, J. T. Kiehl, and D. Rosenfeld, 2001: Aerosols, climate, and the hydrological cycle. *Science*, **294**, 2119–2124, https://doi.org/10.1126/science.1064034.

Rasmussen, R., C. Liu, K. Ikeda, D. Gochis, D. Yates, F. Chen, and K. Miller, 2011: High-resolution coupled climate runoff simulations of seasonal snowfall over Colorado: A process study of current and warmer climate. *J. Climate*, **24**, 3015–3048, https://doi.org/10.1175/2010JCLI3985.1.

Reif, D. W., H. B. Bluestein, 2017: A 20-year climatology of nocturnal convection initiation over the central and southern Great Plains during the warm season. *Mon. Wea. Rev.*, **145**, 1615–1639, https://doi.org/10.1175/MWR-D-16-0340.1.

Riahi, K., and Coauthors, 2011: RCP 8.5—A scenario of comparatively high greenhouse gas emissions. *Climatic Change*, **109**, 33–57, https://doi.org/10.1007/s10584-011-0149-y.

Rinehart, R. E., 2004: *Radar for Meteorologists*. University of North Dakota, 482 pp.

Rummukainen, M., 2009: State-of-the-art with regional climate models. *WIREs Climate Change*, **1**, 82–96, https://doi.org/10.1002/wcc.8.

Schär, C., C. Frei, D. Lüthi, and H. C. Davies, 1996: Surrogate climate-change scenarios for regional climate models. *Geophys. Res. Lett.*, **23**, 669–672, https://doi.org/10.1029/96GL00265.

Skamarock, W. C., J. B. Klemp, J. Dudhia, D. O. Gill, M. Barker, K. G. Duda, X. Y. Huang, W. Wang, J. G. Powers, 2008: A description of the advanced research WRF version 3. http://www2.mmm.ucar.edu/wrf/users/docs/arw_v3.pdf.

Song, J., K. Liao, R. L. Coulter, and B. M. Lesht, 2005: Climatology of the low-level jet at the southern Great Plains atmospheric boundary layer experiments site. *J. Appl. Meteor.*, **44**, 1593–1606, https://doi.org/10.1175/JAM2294.1.

Steiner, M., R. A. Houze, and S. E. Yuter, 1995: Climatological characterization of three-dimensional storm structure from operational radar and rain gauge data. *J. Appl. Meteor.*, **34**, 1978–2007, https://doi.org/10.1175/1520-0450(1995)034%3C1978:CCOTDS%3E2.0.CO;2.

Stelten, S., W. A. Gallus, 2017: Pristine nocturnal convective initiation: A climatology and preliminary examination of predictability. *Wea. Forecasting*, **32**, 1613–1635, https://doi.org/10.1175/WAF-D-16-0222.1.

Stigler, S. M. 1989: Francis Galton's account of the invention of correlation. *Statistical Science*, **4**,

73-79.

Stoelinga, M. T., P. V. Hobbs, C. F. Mass, J. D. Locatelli, B. A. Colle, R. A. Houze, and G. Thompson, 2003: Improvement of microphysical parameterization through observational verification experiment. *Bull. Amer. Meteor. Soc.*, **84**, 1807–1826, https://doi.org/10.1175/BAMS-84-12-1807.

Stone, D. A., A. J. Weaver, and F. W. Zwiers, 2000: Trends in Canadian precipitation intensity. *Atmosphere-Ocean*, **38**, 321–347, https://doi.org/10.1080/07055900.2000.9649651.

Sui, C. H., X. Li, and K. M. Lau, 1998: Radiative–Convective Processes in Simulated Diurnal Variations of Tropical Oceanic Convection. *J. Atmos. Sci*., **55**, 2345–2357, https://doi.org/10.1175/1520-0469(1998)055%3C2345:RCPISD%3E2.0.CO;2.

Surcel, M., M. Berenguer, I. Zawadzki, 2010: The diurnal cycle of precipitation from continental radar mosaics and numerical weather prediction models. Part I: Methodology and seasonal comparison. *Mon. Wea. Rev.*, **138**, 3084–3106, https://doi.org/10.1175/2010MWR3125.1.

Teutschbein, C. and J. Seibert, 2012: Bias correction of regional climate model simulations for hydrological climate-change impact studies: Review and evaluation of different methods. *J. Hydrol.*, **456–457**, 12–29, https://doi.org/10.1016/j.jhydrol.2012.05.052.

Thompson, G, Eidhammer T (2014) A study of aerosol impacts on clouds and precipitation development in a large winter cyclone. *J Atmos Sci*, **71**, 3636–3658, https://doi.org/10.1175/JAS–D–13–0305.1.

Ting, M., and H. Wang, 2006: The role of the North American topography on the maintenance of the Great Plains summer low-level jet. *J. Atmos. Sci.*, **63**, 1056–1068, https://doi.org/10.1175/JAS3664.1.

Trenberth, K. E., A. Dai, R. M. Rasmussen, D. B. Parsons, 2003: The changing character of precipitation. *Bull. Amer. Meteor. Soc.*, **84**, 1205–1218, https://doi.org/10.1175/BAMS-84-9-1205.

Trier, S. B., C. A. Davis, and D. A. Ahijevych, 2010: Environmental controls on the simulated diurnal cycle of warm-season precipitation in the continental United States. *J. Atmos. Sci.*, **67**, 1066–1090, https://doi.org/10.1175/2009JAS3247.1.

Tucker, D. F., N. A. Crook, 1999: The generation of mesoscale convective system from mountain convection. *Mon. Wea. Rev.*, **127**, 1259–1273, https://doi.org/10.1175/1520-0493(1999)127%3C1259:TGOAMC%3E2.0.CO;2.

Tuttle, J. D., and C. A. Davis, 2006: Corridors of warm season precipitation in the central United

States. *Mon. Wea. Rev.*, **134**, 2297–2317, https://doi.org/10.1175/MWR3188.1.

UK Met Office, 2012: National Meteorological Library and Archive Fact sheet 3 — Water in the atmosphere. Accessed 12 March 2019, https://www.metoffice.gov.uk/binaries/content/assets/mohippo/pdf/f/c/fact_sheet_no._3.pdf.

Walpole, R. E., R. H. Myers, S. L. Myers, and K. Ye, 2012: *Probability & Statistics for Engineers & Scientists*. Prentice Hall, 791 pp.

Watson, R. T., M. C. Zinyowera, R. H. Moss, and D. J. Dokken, 1998: The regional impacts of climate change. An assessment of vulnerability: A Special Report of IPCC Working Group II, 517.

Wetzel, P. J., W. R. Cotton, and R. L. McAnelly, 1983: A long-lived mesoscale convective complex. Part II: Evolution and structure of the mature complex. *Mon. Wea. Rev.*, **111**, 1919–1937, https://doi.org/10.1175/1520-0493(1983)111%3C1919:ALLMCC%3E2.0.CO;2.

Willett, K. M., N. P. Gillett, P. D. Jones, and P. W. Thorne, 2007: Attribution of observed surface humidity changes to human influence. *Nature*, **449**, 710–712, https://doi.org/10.1038/nature06207.

Winterfeldt, J., R. Weisse, 2009: Assessment of Value Added for Surface Marine Wind Speed Obtained from Two Regional Climate Models. *Mon. Wea. Rev.*, **137**, 2955–2965, https://doi.org/10.1175/2009MWR2704.1.

Yang, Y., X. Chen, and Y. Qi, 2013: Classification of convective/stratiform echoes in radar reflectivity observations using a fuzzy logic algorithm. *J. Geophys. Res.*, **118**, 1896–1905, https://doi.org/10.1002/jgrd.50214.

Appendix

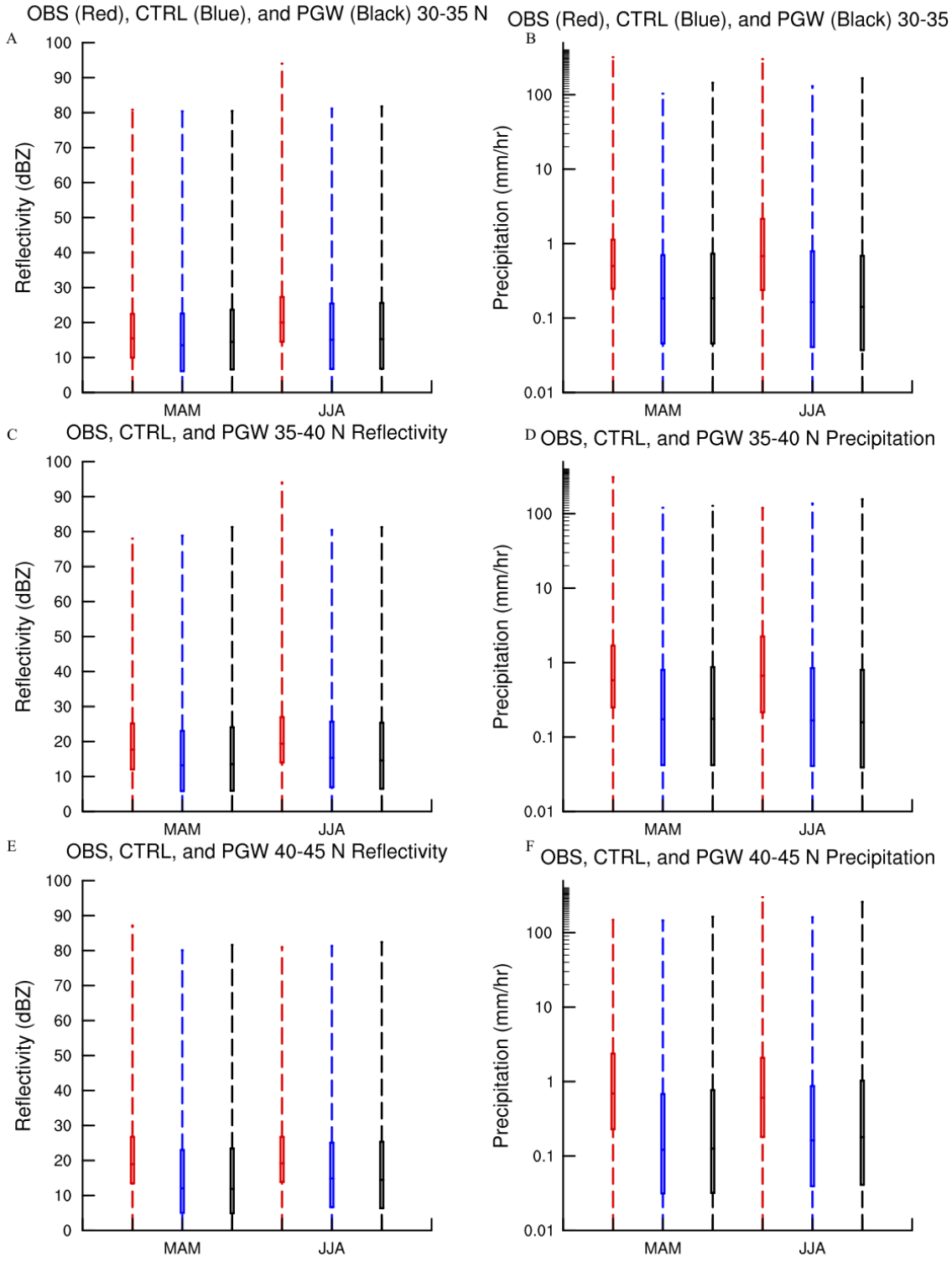

Figure A.1: Precipitation rate (right) and reflectivity (left) box plots for observations, WRF CTRL, and WRF PGW during MAM and JJA for values above 15 dBZ and 0.3 mm hr^{-1} for R1, R2, and R3 (top to bottom).